Experimental Test of Lepton Universality in tau Decay

Submitted to Physical Review D

Stanford Linear Accelerator Center, Stanford University, Stanford, CA 94309

Experimental tests of lepton universality in tau decay

CLEO Collaboration

(December 19, 1996)

Abstract

The branching fractions for $\tau \to e\nu\nu_\tau$, $\mu\nu\nu_\tau$, and $h\nu_\tau$ are measured using data collected with the CLEO detector at the CESR e^+e^- collider: $\mathcal{B}_e$=0.1776±0.0006±0.0017, $\mathcal{B}_\mu$=0.1737±0.0008±0.0018, and $\mathcal{B}_h$=0.1152±0.0005±0.0012, where the first error is statistical, the second systematic, and h refers to either a charged π or K. Also measured is the tau mass, m_τ=(1778.2±1.4) MeV. Lepton universality is affirmed by the relative branching fractions ($\mathcal{B}_\mu/\mathcal{B}_e$=0.9777±0.0063±0.0087, $\mathcal{B}_h/\mathcal{B}_e$=0.6484±0.0041±0.0060) and the charged-current gauge coupling-constant ratios (g_μ/g_e=1.0026±0.0055, g_τ/g_μ=0.9990±0.0098). The tau mass result may be recast as a tau neutrino mass limit, m_{ν_τ}<60 MeV at 95% CL.

Typeset using REVT_EX

A. Anastassov,[1] S. Blinov,[1,*] J. E. Duboscq,[1] K. D. Fisher,[1] D. Fujino,[1,†] R. Fulton,[1]
K. K. Gan,[1] T. Hart,[1] K. Honscheid,[1] H. Kagan,[1] R. Kass,[1] J. Lee,[1] M. B. Spencer,[1]
M. Sung,[1] A. Undrus,[1,*] R. Wanke,[1] A. Wolf,[1] M. M. Zoeller,[1] B. Nemati,[2] S. J. Richichi,[2]
W. R. Ross,[2] P. Skubic,[2] M. Wood,[2] M. Bishai,[3] J. Fast,[3] E. Gerndt,[3] J. W. Hinson,[3]
N. Menon,[3] D. H. Miller,[3] E. I. Shibata,[3] I. P. J. Shipsey,[3] M. Yurko,[3] L. Gibbons,[4]
S. D. Johnson,[4] Y. Kwon,[4] S. Roberts,[4] E. H. Thorndike,[4] C. P. Jessop,[5] K. Lingel,[5]
H. Marsiske,[5] M. L. Perl,[5] S. F. Schaffner,[5] D. Ugolini,[5] R. Wang,[5] X. Zhou,[5] T. E. Coan,[6]
V. Fadeyev,[6] I. Korolkov,[6] Y. Maravin,[6] I. Narsky,[6] V. Shelkov,[6] J. Staeck,[6]
R. Stroynowski,[6] I. Volobouev,[6] J. Ye,[6] M. Artuso,[7] A. Efimov,[7] F. Frasconi,[7] M. Gao,[7]
M. Goldberg,[7] D. He,[7] S. Kopp,[7] G. C. Moneti,[7] R. Mountain,[7] Y. Mukhin,[7] S. Schuh,[7]
T. Skwarnicki,[7] S. Stone,[7] G. Viehhauser,[7] X. Xing,[7] J. Bartelt,[8] S. E. Csorna,[8] V. Jain,[8]
S. Marka,[8] A. Freyberger,[9] D. Gibaut,[9] R. Godang,[9] K. Kinoshita,[9] I. C. Lai,[9]
P. Pomianowski,[9] S. Schrenk,[9] G. Bonvicini,[10] D. Cinabro,[10] R. Greene,[10] L. P. Perera,[10]
B. Barish,[11] M. Chadha,[11] S. Chan,[11] G. Eigen,[11] J. S. Miller,[11] C. O'Grady,[11]
M. Schmidtler,[11] J. Urheim,[11] A. J. Weinstein,[11] F. Würthwein,[11] D. M. Asner,[12]
D. W. Bliss,[12] W. S. Brower,[12] G. Masek,[12] H. P. Paar,[12] M. Sivertz,[12] V. Sharma,[12]
J. Gronberg,[13] R. Kutschke,[13] D. J. Lange,[13] S. Menary,[13] R. J. Morrison,[13] H. N. Nelson,[13]
T. K. Nelson,[13] C. Qiao,[13] J. D. Richman,[13] D. Roberts,[13] A. Ryd,[13] M. S. Witherell,[13]
R. Balest,[14] B. H. Behrens,[14] K. Cho,[14] W. T. Ford,[14] H. Park,[14] P. Rankin,[14] J. Roy,[14]
J. G. Smith,[14] J. P. Alexander,[15] C. Bebek,[15] B. E. Berger,[15] K. Berkelman,[15] K. Bloom,[15]
D. G. Cassel,[15] H. A. Cho,[15] D. M. Coffman,[15] D. S. Crowcroft,[15] M. Dickson,[15]
P. S. Drell,[15] K. M. Ecklund,[15] R. Ehrlich,[15] R. Elia,[15] A. D. Foland,[15] P. Gaidarev,[15]
R. S. Galik,[15] B. Gittelman,[15] S. W. Gray,[15] D. L. Hartill,[15] B. K. Heltsley,[15]
P. I. Hopman,[15] J. Kandaswamy,[15] N. Katayama,[15] P. C. Kim,[15] D. L. Kreinick,[15] T. Lee,[15]
Y. Liu,[15] G. S. Ludwig,[15] J. Masui,[15] J. Mevissen,[15] N. B. Mistry,[15] C. R. Ng,[15]
E. Nordberg,[15] M. Ogg,[15,‡] J. R. Patterson,[15] D. Peterson,[15] D. Riley,[15] A. Soffer,[15]
C. Ward,[15] M. Athanas,[16] P. Avery,[16] C. D. Jones,[16] M. Lohner,[16] C. Prescott,[16] S. Yang,[16]
J. Yelton,[16] J. Zheng,[16] G. Brandenburg,[17] R. A. Briere,[17] Y.S. Gao,[17] D. Y.-J. Kim,[17]
R. Wilson,[17] H. Yamamoto,[17] T. E. Browder,[18] F. Li,[18] Y. Li,[18] J. L. Rodriguez,[18]
T. Bergfeld,[19] B. I. Eisenstein,[19] J. Ernst,[19] G. E. Gladding,[19] G. D. Gollin,[19]
R. M. Hans,[19] E. Johnson,[19] I. Karliner,[19] M. A. Marsh,[19] M. Palmer,[19] M. Selen,[19]
J. J. Thaler,[19] K. W. Edwards,[20] A. Bellerive,[21] R. Janicek,[21] D. B. MacFarlane,[21]
K. W. McLean,[21] P. M. Patel,[21] A. J. Sadoff,[22] R. Ammar,[23] P. Baringer,[23] A. Bean,[23]
D. Besson,[23] D. Coppage,[23] C. Darling,[23] R. Davis,[23] N. Hancock,[23] S. Kotov,[23]
I. Kravchenko,[23] N. Kwak,[23] S. Anderson,[24] Y. Kubota,[24] M. Lattery,[24] J. J. O'Neill,[24]
S. Patton,[24] R. Poling,[24] T. Riehle,[24] V. Savinov,[24] A. Smith,[24] M. S. Alam,[25]
S. B. Athar,[25] Z. Ling,[25] A. H. Mahmood,[25] H. Severini,[25] S. Timm,[25] and F. Wappler[25]

---

*Permanent address: BINP, RU-630090 Novosibirsk, Russia.

†Permanent address: Lawrence Livermore National Laboratory, Livermore, CA 94551.

‡Permanent address: University of Texas, Austin TX 78712

[1]Ohio State University, Columbus, Ohio 43210

[2]University of Oklahoma, Norman, Oklahoma 73019

[3]Purdue University, West Lafayette, Indiana 47907

[4]University of Rochester, Rochester, New York 14627

[5]Stanford Linear Accelerator Center, Stanford University, Stanford, California 94309

[6]Southern Methodist University, Dallas, Texas 75275

[7]Syracuse University, Syracuse, New York 13244

[8]Vanderbilt University, Nashville, Tennessee 37235

[9]Virginia Polytechnic Institute and State University, Blacksburg, Virginia 24061

[10]Wayne State University, Detroit, Michigan 48202

[11]California Institute of Technology, Pasadena, California 91125

[12]University of California, San Diego, La Jolla, California 92093

[13]University of California, Santa Barbara, California 93106

[14]University of Colorado, Boulder, Colorado 80309-0390

[15]Cornell University, Ithaca, New York 14853

[16]University of Florida, Gainesville, Florida 32611

[17]Harvard University, Cambridge, Massachusetts 02138

[18]University of Hawaii at Manoa, Honolulu, Hawaii 96822

[19]University of Illinois, Champaign-Urbana, Illinois 61801

[20]Carleton University, Ottawa, Ontario, Canada K1S 5B6
and the Institute of Particle Physics, Canada

[21]McGill University, Montréal, Québec, Canada H3A 2T8
and the Institute of Particle Physics, Canada

[22]Ithaca College, Ithaca, New York 14850

[23]University of Kansas, Lawrence, Kansas 66045

[24]University of Minnesota, Minneapolis, Minnesota 55455

[25]State University of New York at Albany, Albany, New York 12222

I. INTRODUCTION

Understanding the origin of electroweak symmetry breaking and the hierarchy of quark and lepton masses is a fundamental goal of elementary particle physics. Tau lepton decays provide a laboratory in which to engage this pursuit. Theory predicts unambiguous and quite simple relationships between the tau lifetime, mass, and several of its branching fractions. Therefore experimental determination of these parameters to the highest possible precision is essential; deviations from the predictions at any level could signal the presence of physics beyond our present understanding. This article describes measurements of the tau mass, its branching fractions to e, μ, and π/K, their relationships to the tau lifetime, and compares the results with predictions.

In what follows, the symbol $\mathcal{B}_a$ signifies the tau branching fraction to the indicated particle, plus one or two neutrinos and radiative photons. In particular, $\mathcal{B}_h \equiv \mathcal{B}_\pi + \mathcal{B}_K$ does not include modes with K_L^0's, which are explicitly treated as backgrounds.

Predicted dependencies among the tau lepton decay parameters are most conveniently expressed in terms of the charged-current gauge coupling strengths g_e, g_μ, and g_τ. Lepton universality, a basic ingredient in the minimal standard model, requires that these couplings be identical: $g_e = g_\mu = g_\tau$. In tau decays, μ-e universality is tested in the ratio of muonic to electronic branching fractions

$$\left(\frac{g_\mu}{g_e}\right)^2 = \frac{f(x_e)}{f(x_\mu)} \frac{B(\tau \to \mu\nu\nu)}{B(\tau \to e\nu\nu)} = \frac{1}{0.9726} \frac{\mathcal{B}_\mu}{\mathcal{B}_e} \tag{1}$$

where B denotes a branching fraction, $x_\ell = (m_\ell/m_\tau)^2$, $f(x) = 1 - 8x + 8x^3 - x^4 - 12x^2 \ln x$, and m_ℓ represents a particle mass. Comparing the electronic decay of the tau with that of the muon probes τ-μ universality:

$$\begin{aligned}
\left(\frac{g_\tau}{g_\mu}\right)^2 &= \frac{\tau_\mu}{\tau_\tau} \left(\frac{m_\mu}{m_\tau}\right)^5 \frac{B(\tau \to e\nu\nu)}{B(\mu \to e\nu\nu)} \\
&\quad \times (1 + \delta_W)(1 + \delta_\gamma) \\
&= 28924 \text{ fs GeV}^5 \ \frac{\mathcal{B}_e}{\tau_\tau \ m_\tau^5}
\end{aligned} \tag{2}$$

where $\delta_W = -2.9 \times 10^{-4}$ and $\delta_\gamma = 8.6 \times 10^{-5}$ are the weak and electromagnetic radiative corrections [1], respectively, and τ_ℓ denotes a particle lifetime. A second measure of τ-μ universality is obtained by comparing the muonic decays of the pion and kaon with the pionic and kaonic decays of the tau:

$$\begin{aligned}
\left(\frac{g_\tau}{g_\mu}\right)^2 &= \frac{2 \ m_\mu^2}{\tau_\tau \ m_\tau^3} \frac{B(\tau \to \pi\nu) + B(\tau \to K\nu)}{H_\pi + H_K} \\
&= 14025 \text{ fs GeV}^3 \ \frac{\mathcal{B}_h}{\tau_\tau \ m_\tau^3}
\end{aligned} \tag{3}$$

where

$$H_h = \frac{1 + \delta_h}{\tau_h \ m_h} \left(\frac{1 - m_h^2/m_\tau^2}{1 - m_\mu^2/m_h^2}\right)^2 B(h \to \mu\nu) \tag{4}$$

4

and δ_π=0.0016$^{+0.0009}_{-0.0014}$ and δ_K=0.0099$^{+0.0017}_{-0.0026}$ are electromagnetic radiative corrections [2,3]. A consequence of Eqs. (2) and (3), independent of τ-μ universality, is the predicted ratio

$$
\begin{aligned}
\frac{\mathcal{B}_h}{\mathcal{B}_e} &= \frac{B(\tau \to \pi\nu) + B(\tau \to K\nu)}{B(\tau \to e\nu\nu)} \\
&= \frac{\tau_\mu \; m_\mu^3}{2 \; m_\tau^2} \left(H_\pi + H_K \right) \left(1 + \delta_W \right) \left(1 + \delta_\gamma \right) \\
&= \left(\frac{1.436 \text{ GeV}}{m_\tau} \right)^2
\end{aligned}
\tag{5}
$$

One or more of the ratios in Eqs. (1−3) will deviate from unity in many extensions of the minimal standard model [4]. The masses, lifetimes, and leptonic branching fractions of the muon, pion, and kaon have all been measured [5] with relative precisions <0.1%, while tau properties remain uncertain at the 1% level. Hence continued refinement of tau lifetime, mass, and branching fraction measurements will constrain such extensions.

The approach taken here is to determine the relevant branching fractions of the tau and its mass using tau-pair decays produced by e^+e^- collisions near $\sqrt{s}$=10.6 GeV at the Cornell Electron Storage Ring (CESR) and measured in the CLEO detector. These results are then combined with a CLEO measurement of the tau lifetime [6] for the lepton universality tests described above. The branching fraction analysis uses nine tau-pair decay modes: ee, $\mu\mu$, hh, $e\mu$, eh, μh, ρe, $\rho\mu$, and ρh, where h is a charged pion or kaon, and ρ signifies an h accompanied by at least one π^0. Initially, carefully chosen selection criteria cull the desired events from the dataset. Then efficiencies and backgrounds are determined using subsets of the data as well as Monte Carlo simulations. The background-subtracted, efficiency-corrected event tallies are normalized to the number of tau-pairs produced. The resulting nine product branching fractions are then fit for individual branching fractions. For the tau mass measurement, the minimum parent mass kinematically allowed is computed for each hh event. The shape of the resulting distribution is fit for m_τ and then combined with a similar previous analysis [7], which employed $\rho\rho$ and $h\rho$ events.

II. APPARATUS

CLEO II [8] is a general purpose detector. A set of three concentric drift chambers in a 1.5 T axial magnetic field measures charged particle trajectories with momentum resolution σ_p/p (%) $\simeq \sqrt{(0.15p)^2 + (0.5)^2}$, p in GeV/c. These chambers have 67 cylindrical drift-cell layers centered on the beam line, with radii from 4.7-90 cm. Track $z-$coordinates [9] are measured with eleven stereo layers and four planes of cathode strips. The beam pipe, chamber walls, gas, and wires together constitute 0.028 radiation lengths of material at normal incidence between the nominal interaction point (IP) and last drift chamber layer. Surrounding the drift chambers, but inside the superconducting magnet coil, a calorimeter of 7800 CsI(Tl) crystals with silicon photodiode readout measures the energy and position of photons and electrons. The 6144 barrel crystals, arranged in a projective geometry, surround the tracking chambers at 1 m radius, covering $|\cos\theta|$<0.82. Two identical endcaps, each containing 828 rectangular crystals, occupy 0.80<$|\cos\theta|$<0.98, and complete the hermetic

coverage over 98% of the solid angle. For electromagnetic showers, the barrel calorimeter achieves energy and angular resolutions, respectively, of $\sigma_E/E(\%)=0.35/E^{0.75} + 1.9 - 0.1E$ and $\sigma_\phi(\text{mrad})=2.8/\sqrt{E} + 2.5$, E in GeV. A photon candidate is defined as any calorimeter shower unassociated with a charged track; a shower is associated with a track if that track's trajectory projects to within 8 cm of any crystal in that shower. Muons are identified by their penetration through the calorimeter, coil, and one or more of three 36 cm-thick slabs of magnet iron; three layers of Iarocci tube chambers instrument the gap behind each slab. Fast trigger signals and particle time-of-flight (TF) are provided by 5 cm-thick scintillation counters located just inside the calorimeter in the barrel and endcap. The 64 barrel TF counters are 279 cm long by 10 cm wide, are aligned parallel to the beams, and are read out by photomultiplier tubes at both ends.

A three-tier hardware trigger system [10] takes input from the calorimeter, tracking chambers, and TF counters to form different combinations of requirements that force readout of the entire detector. At the lowest level trigger, L0, simple and fast criteria reduce the 2.7 MHz beam-crossing frequency to a manageable rate (10 KHz). The more complex logical conditions that are input at the next level, L1, are ready for interrogation about 1 μs later, and reduce the rate much further (50 Hz). The readiness time for the third level, L2, is approximately 50 μs, eliminating about half the L1 triggers. A fourth-level trigger (L3) implemented in software processes information assembled from the entire detector to reject about half the L2 triggers as uninteresting cosmic rays or interactions of the beam particles with gas or vacuum chamber walls. Every 200-th event failing L2 and every eighth failing L3 criteria are tagged but retained in the data stream for subsequent monitoring of trigger performance.

Every trigger must fire either a "2TF" or "TF*VD" at L0, the former requiring two non-adjacent barrel TF counters, and the latter a single TF counter accompanied by a fast-hardware-track found in CLEO's 10-layer intermediate drift chamber (VD). At L1 and L2, there are two hardware triggers directly relevant to this analysis. The first, ELTRK, is designed to select events with a moderately energetic shower and at least one track. ELTRK requires one TF counter (or two, in part of the data sample), enough drift chamber hits to satisfy a hardware track-finder, and a "Crystal-Barrel-HIgh" (CBHI) calorimeter signal: at least 0.5 GeV deposited in one or more 4×4 grouping of calorimeter crystals. The second, 2TRK, is designed to fire for events with two or more tracks leaving minimum-ionizing showers in the calorimeter, which typically deposit 0.220 GeV. 2TRK requires two struck TF counters, two hardware-track-finder tracks, and two non-adjacent "Crystal-Barrel-Low" (CBLO) calorimeter signals (an energy deposition exceeding 0.1 GeV in a 4×4 crystal grouping). A third trigger, known as ENERGY, is useful for efficiency studies: it requires two CBHI calorimeter signals in opposite $z-$hemispheres separated by at least 90° in azimuth.

III. EVENT SELECTION

We choose events with two charged particles in the barrel region of the detector, where the precision for charged track measurement and lepton identification is optimal. To suppress backgrounds with photons such as $\ell\ell\gamma$ ($\ell\equiv e/\mu$) and tau decays containing extra π^0's, calorimeter activity unrelated to the charged particles is restricted. For $\ell\ell\gamma$ and $ee\ell\ell$ back-

grounds, the momentum of any unseen particle(s) frequently points parallel to the beam direction, unlike the neutrinos in tau-pair events. Therefore requiring a non-zero missing momentum that points into the detector enhances tau-pair events relative to these backgrounds. Cosmic rays are almost completely eliminated by requiring the two charged tracks to be acollinear and to originate near the IP. Stringent particle identification and limitations upon observed photons are imposed to minimize tau-pair feed-across subtractions. Specific hardware trigger criteria with high and measurable efficiencies are chosen for each mode.

We do not distinguish between charged pions and kaons to eliminate the systematic error that would result from explicit identification. The ρ-tagged modes are included to obtain more statistics for e, μ, and h decays; the $\tau \to h\pi^0\nu$ branching fraction has been measured [11] previously using the CLEO dataset and is not updated here.

Selected events must have exactly two good charged particle tracks. At this stage a good track is defined as having momentum $p_\pm > 0.15$ GeV/c or impact parameter max$|d_\pm| < 10$ mm, where $d_\pm$ is the signed distance of closest approach to the IP in the plane transverse to the beam. This requirement allows photon conversions, knock-on electrons, or "junk" tracks (most of which occur at low $p_\pm$ and/or large $|d_\pm|$) to be present, and henceforth ignored. The two good tracks are subsequently required to be of opposite charge, have momenta scaled to the beam energy $x_\pm \equiv p_\pm/E_b$ satisfying $0.1 < x_\pm < 0.9$, impact parameters $|d_\pm| < 2$ mm, and $|\cos\theta_\pm| < 0.7$. If we define the acoplanarity $\xi \equiv ||\phi_+ - \phi_-| - \pi|$ as the two-track acollinearity in azimuth, $x_t \equiv p_t/E_b$ as the component of missing momentum transverse to the beam, scaled to the beam energy, and $|\cos\theta_{mis}|$ as the direction of this missing momentum, the two tracks must have $0.05 < \xi < 1.5$, $x_t > 0.1$, and $|\cos\theta_{mis}| < 0.8$.

The "ρ-tag" is defined to have an energetic π^0 in the same hemisphere as a track not identified as a lepton. To ensure a high trigger efficiency, at least one of the photons in the π^0 must have scaled energy $x_\gamma \equiv E_\gamma/E_b > 0.2$. The other photon must satisfy $x_\gamma > 0.01$, and the two-photon invariant mass must lie in the range $0.100 < M_{\gamma\gamma} < 0.160$ GeV. Both photons must satisfy $|\cos\theta_\gamma| < 0.7$. The momentum of the ρ (not the track) is used to compute x_t and $|\cos\theta_{mis}|$; for ρ-tag modes, no restriction is made upon $|\cos\theta_{mis}|$, and the missing transverse momentum requirement is loosened to $x_t > 0.05$. To discriminate against non-tau backgrounds, we require $M_s < 1.8$ GeV on the ρ-side of the event, where the variable M_s is defined as the invariant mass of one side of the event: a track (assuming a pion mass) plus all photon candidates nearer that track than the other and which have $|\cos\theta_\gamma| < 0.9$. Events with additional neutrals on the ρ-side are included in the signal, so that several tau decay modes can contribute to the "ρ" tag: $\rho \to \pi\pi^0$, $a_1 \to \pi 2\pi^0$, $K^* \to K\pi^0$, $K^* \to \pi K_S (\to 2\pi^0)$, etc.

Radiative QED backgrounds and tau decay modes with energetic π^0's are discriminated against by requiring any detected photons, excluding those in an identified ρ-tag, to have scaled energy $x_\gamma < 0.10$. To exclude events in which a photon hides in a track's calorimeter shower, each track's calorimeter-energy-to-momentum ratio must satisfy $E_\pm/p_\pm < 1.1$. This requirement eliminates Bhabha events (in which one track radiates a photon) and tau-pair feed-across (in which a photon from an unwanted π^0 randomly overlaps a track's shower).

Further limitations on extra showers depends upon the species of the nearest charged particle. Any shower nearest in angle to an identified lepton must satisfy $x'_\gamma < 0.01$ if it is likely to be a true, event-related photon, which is defined as $|\cos\theta_\gamma| < 0.8$, shower location more than 20 cm from both charged tracks' projected entry points into the calorimeter, and a lateral profile consistent with that of a photon shower. To reduce dependence upon

the simulation of hadronic interactions in the calorimeter, which affects the population of photon candidates, a different strategy is employed on the h-side of an event: we require $M_s < 0.4$ GeV. This tends to eliminate backgrounds from tau decays to higher mass states with at least one π^0 accompanying the h (ρ, a_1, K^*, etc.) and is well-modeled by the Monte Carlo simulation.

Electron and muon identification criteria establish for each charged track, with some probability, its identity as an e, μ, or h. The symbol h represents π or K, and is defined operationally as "not identified a lepton". The criteria are chosen to have high efficiencies for signal modes and small backgrounds from non-signal tau-decay modes. Electrons are identified with scaled momenta $x_\pm > 0.1$; muons and hadrons with $x_\pm > 0.285$. Electron criteria require that $E_\pm / p_\pm > 0.85$, and that its drift chamber specific-ionization (dE/dx) be no lower than two standard deviations below that expected for an electron. Muon criteria demand that the track deposit $E_\pm < 0.6$ GeV in the calorimeter, consistent with a minimum-ionizing particle, and that there be hits in the muon detection system matched to the projected trajectory of the track. The muon chamber hits must be consistent with a penetration of at least three hadronic interaction lengths for $p_\pm < 2.0$ GeV/c and five interaction lengths for $p_\pm > 2.0$ GeV/c. The two depths correspond to the first and second superlayers of muon chambers. Allowing a smaller penetration depth for lower momentum avoids a rapid reduction in efficiency and the associated larger uncertainty.

Additional criteria address differing mode-specific needs. For high efficiency triggering on calorimeter energy in $e\mu$ and eh events, the electron scaled momentum must satisfy $x_\pm > 0.235$. To suppress $ee\gamma$ and $\mu\mu\gamma$ contamination, the scaled energy must satisfy ($x_+ + x_-$) < 1.5 for the ee and $\mu\mu$ modes. For reliable triggering, the two tracks in $\mu\mu$, μh, and hh events must be in opposite z hemispheres; i.e., $\cos\theta_+ \times \cos\theta_- < 0$. The hardware trigger known as ELTRK must have fired for ee, $e\mu$, eh, and all ρ-tag modes; each of these modes features at least one energetic shower nearly guaranteed to satisfy the calorimeter portion of this trigger. For the $\mu\mu$ mode, the trigger known as 2TRK is required. Events in the μh and hh modes must have fired either ELTRK or 2TRK.

The $\ell\ell\gamma\gamma$ and $ee\ell\ell$ processes can survive the above selection criteria if the unseen pair of radiative photons or electrons combine to yield a missing momentum pointing into the detector. To eliminate this possibility we define a new variable as the missing transverse momentum divided by the missing energy:

$$\sin\Theta_{\min} \equiv \frac{x_t}{2 - x_+ - x_-} \tag{6}$$

Energy-momentum conservation makes $\Theta_{\min}$ the minimum polar angle of any unseen particles. For the ee and $\mu\mu$ modes, we require $\Theta_{\min} > 0.18$, because calorimeter coverage extends to this polar angle. Combining this requirement with the x_γ and x'_γ limitations forces unseen particles to traverse the calorimeter without a significant energy deposition, which for a hermetic, efficient detector means they cannot be energetic electrons or photons.

8

IV. BRANCHING FRACTION ANALYSIS

Product branching fractions for tau-pair decays to the final state ab are computed as

$$\mathcal{B}_a \times \mathcal{B}_b = \frac{n \times (1-f)}{(\mathcal{T} \times \mathcal{P} \times \mathcal{A}) \times N_{\tau\tau} \times (2-\delta_{ab})} \tag{7}$$

where n is the total number of events in the specified mode, f is the fractional background in the sample from tau and non-tau sources, including those due to particle misidentification; the efficiency $\mathcal{A} \times \mathcal{P} \times \mathcal{T}$ for selecting the final state ab includes effects of triggering ($\mathcal{T}$), particle identification ($\mathcal{P}$), and acceptance ($\mathcal{A}$); $N_{\tau\tau}$ is the total number of tau-pairs produced by ee collisions during data-taking; and the Kronecker-δ accounts for the case when $a=b$ (i.e., the ee, $\mu\mu$, and hh modes). The measured event tallies, efficiencies, backgrounds, and resulting product branching fractions are shown in Table I along with their errors. The two errors on each product branching fraction represent, first, the statistical error due to the number of events found in the data, and second, the systematic error, due to all other sources combined in quadrature. The methods used to determine the entries in Table I are explained below.

A. Normalization

The number of tau-pairs is computed as the product of the tau-pair cross section and the integrated luminosity, summed over all runs,

$$N_{\tau\tau} = \sum_i \left\{ \sigma_0(s_i) \times (1+\delta_\tau) \right\} \times \mathcal{L}_i \tag{8}$$

in which $\sigma_0(s_i)$ is the point cross section evaluated at the square of the center-of-mass energy s_i,

$$\sigma_0(s_i) \equiv \frac{86.856 \text{ nb GeV}^2}{s_i} \, , \tag{9}$$

the integrated luminosity $\mathcal{L}_i$ is measured [12] using wide angle Bhabha, μ-pair, and $\gamma\gamma$ final states with a relative error of 1%, and the theoretical factor adjusting the point cross section for non-zero tau mass effects and initial and final state radiative corrections [13] is $(1+\delta_\tau)$=1.1732, also with a relative error of 1%. Hence the total integrated luminosity of 3.555 fb^{-1}, accumulated near two beam energies, 68.05% at E_b=5.29 GeV and the balance at 5.26 GeV, corresponds to $N_{\tau\tau}$=(3.250±0.046)×10^6. Theoretical uncertainties in radiative corrections for $\gamma\gamma$, ee, $\mu\mu$, and $\tau\tau$ final states dominate the error in $N_{\tau\tau}$.

B. Monte Carlo samples

For efficiencies and tau-pair feed-across, 10^7 Monte Carlo tau-pairs were generated and decayed with the KORALB [13] program coupled to a detector simulation based on GEANT [14], equivalent to 3.318 times the luminosity of the acquired data. The tau branching fractions used in this Monte Carlo generation are consistent with world-average measurements [5]. Additional events were generated in some modes (ee, $e\mu$, eh, and $\mu\mu$) to reduce the statistical error on the acceptance.

C. Efficiencies

The efficiency with which events are found and classified as one of the chosen tau-pair decay modes is expressed as the product of three distinct factors, which separately account for the trigger efficiency, particle identification, and acceptance. Acceptance includes the effect of all selection criteria other than trigger and particle identification. The particle identification and trigger efficiencies are determined from data (folded with simulated kinematic distributions), whereas the acceptance is estimated almost entirely using the Monte Carlo simulations.

1. Trigger efficiency

The trigger efficiency $\mathcal{T}$ for each mode is calculated by computing each of several independent (and therefore multiplicative) sub-efficiencies using the data alone. These sub-efficiencies separate naturally into factors accounting for TF, crystal, tracking, and L3 components relevant for each mode. Measured trigger efficiency components are shown in Table II, in which the modes are grouped by trigger requirements: ELTRK (the top six), 2TRK ($\mu\mu$), and the inclusive-OR of ELTRK and 2TRK (μh, hh). For the 2TRK efficiencies only the product of the TF and crystal efficiencies is measured because the gaps between adjacent TF counters aligns with the borders between crystal groupings, causing a correlation precluding direct (and unnecessary) determination of the separate factors.

The 2TF counter efficiency when both tracks are away from counter edges can be measured using the subset of each mode that satisfies a 1TF criterion. This amounts to an inefficiency of 0.3% for the ELTRK trigger modes, as shown in the "TF-ctr" column of Table II. The remaining TF inefficiency is attributable to loss of pulse height for tracks entering a counter near its azimuthal edges. It is calculated mode-by-mode by examining the distributions of the projected charged particle's azimuthal intercept, modulo a half-TF counter width, and quantifying the deficit near the counter edge relative to its center. The inefficiency due to TF counter edge effects is 0.2-1.0%, as shown in the "TF-edge" column in Table II. Thus defined, the two TF efficiencies are independent.

The CBHI efficiency as a function of shower energy is calculated using $\mu\mu\gamma$ events triggering on 2TRK. In this study the muons are restricted to energy depositions below 0.3 GeV so they could not fire CBHI. For shower energies above x_γ=0.2 (1 GeV), the efficiency is constant at (99.80±0.03)%; below x_γ=0.2 it falls off rapidly. This result is verified by lower statistics studies using the photons from π^0's in ρe and $\rho\mu$ events. All the ELTRK trigger modes feature at least one calorimeter shower on the plateau, i.e., with energy in excess of 1 GeV. A systematic error of ±0.15% is assigned to this efficiency for ELTRK trigger modes, as shown in the "Crystal" column in Table II.

Tracking-trigger efficiencies are determined by measuring what fraction of ee, ρe, or $\rho\rho$ events that fire the ENERGY trigger also satisfy the relevant tracking-trigger criteria. A muon is assumed to have the same efficiency as a pion within the errors; the efficiencies show that an electron only has about 0.1% higher efficiency than a pion. The tracking-trigger efficiency losses are about 2% for ELTRK requirements and about 7% for 2TRK, as shown in the "Track" column in Table II. The momentum dependence of these efficiencies is small.

The correlated TF*CBLO efficiency product for a μ (h) is determined by measuring the fraction of single-TF ELTRK triggers that have 2TF*2CBLO on $e\mu$ (eh) events. The electron, restricted to $\phi_{TF} > 0.25$ to ensure firing a TF, has fired a CBLO by virtue of its deposited energy. The additional efficiency in the μh and hh samples from ELTRK triggers, where a single CBHI is required instead of 2CBLO, is due to events in which an h interacts and showers in the calorimeter, and is also computed from the data. The resulting 2TF*2CBLO efficiencies, shown in the "Crystal" column of Table II, range from 89-94%.

The L3 efficiency is computed by counting the number of events in each mode that are tagged as being L3 rejects. These tagged events comprise one-eighth of the events slated for elimination at L3, but were retained in the data stream for only 74% of the total dataset. Hence for each such L3 tagged event found in each mode, there were an additional 7/0.74=9.5 events eliminated at L3. L3 efficiency losses range from none (ee) to 5% ($\mu\mu$).

The efficiencies shown in Table II are averages over the entire dataset used for this analysis, but are not constant over all run periods. Variations of several percent in the hardware tracking and TF*CBLO efficiencies have been observed for several contiguous subsets of the data. These variations have been found to correspond to changes in the trigger components themselves or in the response of detectors to CESR beam conditions.

2. Particle identification efficiency

All particle identification probabilities are measured using subsets of the CLEO dataset with tracks tagged as leptons or hadrons (see Appendix). The efficiencies $P(e{\rightarrow}e){\approx}(97.7{\pm}0.15)\%$ and $P(\mu{\rightarrow}\mu){\approx}(93.0{\pm}0.30)\%$ are measured with radiative lepton-pairs and two-photon events from the data. Lepton efficiencies are determined in bins of momentum and polar angle. A by-product of these efficiencies are the lepton-faking-hadron rates $P(\ell{\rightarrow}h){=}1 - P(\ell{\rightarrow}\ell)$, which are, averaged over momentum, approximately $(2.3{\pm}0.15)\%$ and $(7.0{\pm}0.30)\%$ for e's and μ's, respectively. The fake rates $P(h{\rightarrow}e){\approx}0.1$-$0.5\%$ and $P(h{\rightarrow}\mu){\approx}1$-$5\%$, both with relative errors of $\pm 15\%$, are measured with $\tau{\rightarrow}h\pi^0\nu$ decays in the data and binned in momentum and charge. Hence the hadron identification probability, averaged over momentum, is $P(h{\rightarrow}h){=}1{-}P(h{\rightarrow}e){-}P(h{\rightarrow}\mu){\approx}(97.7{\pm}0.3)\%$.

To determine the net two-particle identification efficiency for a given tau-pair decay mode, for each Monte Carlo signal event we find the identification probabilities for both tracks, as tabulated by particle species, momentum, polar angle, and charge. The product of these probabilities is then averaged over all generated signal events. The resulting value of $\mathcal{P}$ varies with mode from 86-96% with an error of 0.3-0.6%.

3. Acceptance

The acceptance is determined by dividing the number of simulated signal events satisfying all the selection criteria by the total number generated. Knowledge of the acceptance is limited by Monte Carlo statistics and by the accuracy of event generation and detector simulation. The latter effect is evaluated by varying the selection criteria over reasonable ranges and monitoring the resulting product branching fractions. The agreement between the data and simulation is excellent in the relevant ranges of important variables (see Section IV E).

11

There are three small corrections obtained by comparison with data distributions. The detector simulation appears to underestimate the width of the $d_\pm$ distribution slightly, so the acceptance is reduced by $(0.1\pm0.1)\%$ of itself in all modes. The high-side tail of the $E_\pm/p_\pm$ distribution for electrons is also underestimated by the simulation, as determined using $e\mu$ and ρe events for which there are no high-$E_\pm/p_\pm$ (i.e., Bhabha) backgrounds. A momentum-dependent correction is applied, and amounts to $(0.2\pm0.1)\%$ per electron. The acceptance is reduced by an additional $(0.20\pm0.15)\%$ of itself to account for a slight overestimate of track reconstruction efficiencies in the simulation.

The total error assigned to the acceptance for each mode is the quadrature sum of the Monte Carlo statistical error, the systematic errors from the three corrections mentioned above, and an additional 1.0% relative error to account for possible systematic effects of the detector simulation or event generator that are beneath the statistical power of the data to probe. Half of the latter error is assumed to be mode-specific and half common to all modes: this error comprises the quadrature sum of 0.7% independent of all other product branching fractions and 0.7% common to all others. Depending upon mode, the value of $\mathcal{A}$ ranges from 3-11%, with total relative errors of about 1.2%.

D. Backgrounds

Table III shows the background fractions due to all sources considered. Feed-across among the signal modes and from other tau-pair decays constitute the dominant backgrounds. These feed-across levels are computed from the tau-pair Monte Carlo sample using the particle identification weights measured in the data, applying signal trigger efficiencies, and normalizing to luminosity. Table IV shows the feed-across level in each mode attributable to the misidentified tau decay indicated in each column. The small fraction of events with double misidentification are included in only one of the columns. The uncertainties in total feed-across are dominated by the errors on particle identification, which are 15% for $P(h{\to}e)$ and $P(h{\to}\mu)$, 8% for $P(e{\to}h)$, and 4% for $P(\mu{\to}h)$, but also include contributions from trigger efficiency, luminosity, and branching fractions. Modes with K_L^0's are considered background and are explicitly subtracted as feed-across [15].

All other backgrounds are heavily suppressed by the selection criteria, and total less than 1% for most modes. Tails of the observed track impact parameter distributions yield estimates of the cosmic ray contamination. Remaining sources rely upon Monte Carlo simulations of $eeee$, [16] $ee\mu\mu$, [17] $ee\tau\tau$, [17] ee, [18,19] and $\mu\mu$ [20] final states. Like-charge events seen in the data are negligibly small, except for the $e\mu$ mode, for which they indicate a 0.13% level of $ee\mu\mu$ contamination. Backgrounds from $ee{\to}q\bar{q}{\to}$hadrons and $ee{\to}\Upsilon(4S){\to}B\bar{B}$ are negligible.

The cross sections for $ee{\to}ee$, $\mu\mu$, $eeee$, and $ee\mu\mu$ are quite large compared to those probed in this analysis. The selection criteria must suppress these processes by factors up to 10^6 to attain sub-1% contaminations. At this level, it is difficult to verify accurate normalization of these processes, their radiative corrections, and simulated detector response. Hence the Monte Carlo predictions for these final states are each normalized to the data in a region outside of, but adjacent to, the nominal allowed region for a given mode. These background processes dominate the event sample in these normalization regions, but tau-pairs and other

sources must be accounted for as well. A scale factor for each process is then obtained which is applied to the predicted backgrounds in each mode. The normalization regions are $(x_+ + x_-) > 1.5$ in the ee mode for Bhabhas, $x_\pm > 0.9$ in the μh mode for μ-pairs, and $\Theta_{\min} < 0.18$ for $eeee$ and $ee\mu\mu$, in the ee and $\mu\mu$ modes, respectively. The resulting scale factors are 2.9 for Bhabhas, 1.6 for μ-pairs, 0.77 for $eeee$, and 0.57 for $ee\mu\mu$. Total relative errors of $\pm 100\%$ conservatively allow for the approximate nature of this procedure.

E. Systematic checks

Distributions in variables relevant to the selection process are modeled well by the simulations, some examples of which are shown in Figs. 1-8. The histograms are normalized to unit area inside the nominal cuts. Variations of the product branching fractions with reasonably altered cuts are consistent with those expected from the assigned statistical and systematic errors.

Suppression of neutral activity in the h-side of events reduces tau-pair feed-across. However, GEANT modeling of hadronic showers in the calorimeter is imperfect in reproduction of every detail of these nuclear interactions. The selection criteria minimize the dependence upon the GEANT's simulation of hadronic interactions by excluding only likely photons in the lepton-side of the event and high invariant mass states on the h-side. The x_γ cut can be tightened to 0.05 without excessive change, but not below. However, for $M_s > 0.4$ GeV, where the dominant portion of feed-across events are located, the data and Monte Carlo distributions match quite well.

The product branching fractions are stable when divided into eleven consecutive datasets of comparable size, which verifies the correct time-dependent trigger efficiency determinations. The combined χ^2 for all nine product branching fractions to be constant for these eleven run periods is 89 for 90 degrees of freedom. The product branching fractions for on-$\Upsilon(4S)$ and below-$\Upsilon(4S)$ data are statistically consistent with each other, confirming the lack of beam energy dependence and the absence of backgrounds from B-decay.

F. Results

The measured product branching fractions can be combined to yield a single result for each of the desired absolute and relative tau branching fractions. Because enough modes are measured simultaneously, no other "tagging mode" branching fraction, with its attendant uncertainty, must enter the calculation from outside sources, as is sometimes the case with measurements of this kind. For the self-tagging modes, this technique effectively halves most of the relative systematic errors, except particle identification uncertainties, which enter on a per track basis, and hence twice per event. Also, some uncertainties cancel in ratios of product branching fractions. These features can be observed in two simple examples: measuring $\mathcal{B}_e$ with ee events, in which one merely takes $\sqrt{\mathcal{B}_e \mathcal{B}_e}$, or with $e\mu$ and $\mu\mu$ events, in which one takes $\mathcal{B}_e \mathcal{B}_\mu / \sqrt{\mathcal{B}_\mu \mathcal{B}_\mu}$. The latter case contrasts with the former in that the uncertainties of two modes, not one, are incurred, but is similar in that the error in $N_{\tau\tau}$ is halved, and only the uncertainty in $P(e \to e)$ enters ($P(\mu \to \mu)$ cancels in the latter case).

13

For each of $\mathcal{B}_e$, $\mathcal{B}_\mu$, $\mathcal{B}_h$, $\mathcal{B}_\mu/\mathcal{B}_e$, and $\mathcal{B}_h/\mathcal{B}_e$, there are six combinations of product branching fractions that are independent (see Tables V−IX). Five separate χ^2-fits, or weighted averages, of the six combinations are performed, properly accounting for the many error correlations. The fitting procedure utilizes the full covariance matrix, correctly including the effects of all important statistical and systematic correlations in the quantities of Eq. (7), for all modes; the error on the weighted average is the weighted quadrature sum of the errors on the six input combinations, but adjusted for effects of correlations. Tables V−IX also show the results of the fits, including the weighted average and error, the χ^2, and the fitting weight of each entry. The reasonable χ^2 values reflect the internal consistency of the product branching fractions, and that there are no significant underestimates of the uncorrelated systematic errors.

Several cross-checks of the fitting methodology and results have been performed. The fit values and errors are not very sensitive to small changes in the weights. When the fits are performed using only the first three methods in each case, the weighted average and errors differ insignificantly from those in the tables; due to correlations in the efficiencies, backgrounds, and normalizations, adding the remaining methods only marginally improves each fit's precision. Similarly, when the first two methods are excluded from the fits, the resulting weighted averages are completely consistent with those in the tables, but with slightly larger errors.

An alternate procedure for extracting the branching fractions is to perform a global χ^2-fit to the product branching fractions simultaneously, again accounting for correlations. The global fit gives nearly identical results (within 0.1%, relative) and errors (within 5%, relative) as the weighted-average technique, and has a χ^2=2.9 for five degrees of freedom. This procedure has also been employed to explore the impact of omitting any single product branching fraction from the fit. Table X shows how much the branching fraction errors increase if any one of the nine modes is ignored. While most individual modes have a non-trivial impact on one or more of the branching fractions, the ee and μh modes being the extremes in this regard, no single mode so dominates the fit as to make the others irrelevant. There is some degree of balance among the modes.

Each of $\mathcal{B}_e$, $\mathcal{B}_\mu$, $\mathcal{B}_h$, $\mathcal{B}_\mu/\mathcal{B}_e$, and $\mathcal{B}_h/\mathcal{B}_e$, is measured with a total relative error of about 1%. Sources of uncertainty are summarized in Table XI. Systematic errors dominate the absolute branching fraction uncertainties, largely due to the error in the normalization $N_{\tau\tau}$. Statistical errors matter more for $\mathcal{B}_\mu/\mathcal{B}_e$ and $\mathcal{B}_h/\mathcal{B}_e$, for which the normalization cancels.

The five fitted quantities are correlated with each other, with Table XII showing the correlation coefficients $r_{ij}\equiv V_{ij}/(\sigma_i\sigma_j)$, where V is the covariance matrix and the $\sigma_i^2=V_{ii}$ are the variances.

This measured value of $\mathcal{B}_e$ is correlated to, consistent with, and supercedes the CLEO result in ref. [21], which utilized the ee mode on a fraction of the dataset used here. The CLEO value reported in ref. [22], which was based on e-vs-3 events taken with a different detector configuration, is independent of the present determination.

V. TAU MASS

The most precise measurement of the tau mass comes from e^+e^- data taken at tau-pair threshold by BES, $m_\tau^{BES}=(1776.96^{+0.18+0.25}_{-0.21-0.17})$ MeV [23]. This result has previously been corroborated by CLEO and ARGUS, both operating in the Υ regime. ARGUS used decays to three charged hadrons to obtain $m_\tau=(1776.3\pm2.4\pm1.4)$ MeV [24]. The published CLEO result [7] selected $h\rho$ and $\rho\rho$ events, and by fitting the distribution of a minimum kinematically allowable tau mass $(m_\tau)_{min}$ for each event, obtained $m_\tau=(1777.8\pm0.7\pm1.7)$ MeV. The largest contribution to the systematic error was attributable to uncertainty in π^0 energy as measured in the electromagnetic calorimeter.

Here we again employ the $(m_\tau)_{min}$-fitting technique but apply it to hh events. In comparison to our $h\rho$, $\rho\rho$ analysis, this strategy retains sensitivity to m_τ, provides a statistically independent sample, and eliminates dependence upon calorimeter calibration because no π^0 reconstruction is necessary. The tradeoffs are that the branching fractions are smaller, more emphasis is placed upon accurate momentum determinations, and special attention must be paid to eliminating QED backgrounds. This analysis is described in more detail in ref. [25].

The method for extracting $(m_\tau)_{min}$ from dihadron events can be described several ways. Energy-momentum conservation allows each hadronic daughter's momentum vector to determine a cone on which the parent τ direction lies, assuming no initial or final state radiation and a single massless unobserved neutrino in each decay. The opening angle of these two cones depends on the value of the parent mass, m_τ. Reflecting one of the two cones through the origin then gives two cones that intersect, in general on more than one ray. The parent mass can be varied until the cones have only one common line of intersection; this then is $(m_\tau)_{min}$, the smallest kinematically allowed value of the parent mass for that event.

Another interpretation of the technique is shown in Fig. 9. The algorithm for finding $(m_\tau)_{min}$ uses the acollinearity of the two hadrons, making its calculation under the assumption that the momentum vectors of the two hadrons lie in the same plane as those of the two parent taus. The figure shows events with various rotations of the dihadron plane with respect to the tau-pair axis. In (a), the two pions are in the same plane as the parent tau directions and the algorithm will correctly obtain $(m_\tau)_{min}=m_\tau$. In (b) and (c) there are non-zero rotations and the algorithm will produce a value of $(m_\tau)_{min}$ that is less than m_τ. Measurement errors, initial state radiation, and non-tau backgrounds can yield events with $(m_\tau)_{min}>m_\tau$, but proper selection criteria can minimize these sources, thereby maintaining a sharp dropoff, or "edge", in the $(m_\tau)_{min}$ distribution near the true value of m_τ. Events from tau-pair feed-across, such as those containing a lepton faking a hadron or an $h\pi^0$ where the π^0 has gone undetected, tend to have low values of $(m_\tau)_{min}$, and therefore do not significantly alter the shape or position of the edge.

The selection criteria are slightly different from those used for the branching fraction hh sample to increase statistics and to reduce backgrounds and feed-across. The allowed polar angle region is enlarged to $|\cos\theta_\pm|<0.8$, and the momentum restriction loosened on the lower end to $x_\pm>0.25$. QED and two-photon processes are suppressed by the additional requirement that $\Theta_{min}>0.105$. Cosmic rays are removed from the data sample by requiring that the time difference of the tracks' signals in the time-of-flight scintillators, if available, be $\delta_t\leq4$ ns. Tracks heading for octant boundaries in the muon system, where most muon veto inefficiency occurs, are rejected unless both the energy and lateral shape of the shower

15

in the calorimeter are uncharacteristic of muons [26,27].

The baseline Monte Carlo sample is generated with m_τ=1777.0 MeV. Unlike our $h\rho$, $\rho\rho$ analysis, a closed-form few-term function is not used to compare the data to the simulation. To avoid binning effects, instead we use the actual shape of the simulation distribution by fitting it to a cubic spline with eight knots. This spline shape is then fit with floating normalization to the data distribution for $(m_\tau)_{min}$, with the only other free parameter being the shift Δm (relative to 1777.0 MeV) along the mass axis. The fit of the spline to the data distribution for $(m_\tau)_{min}$ is shown in Fig. 10. The fitting range of 1.54-1.86 GeV is chosen to minimize sensitivity to small shifts in the range limits. The resulting mass shift and associated statistical uncertainty is Δm=(+1.5±1.6) MeV. An investigation of systematic effects attributes errors (in MeV) to simulation statistics (0.8), non-tau backgrounds and feed-across (0.7), momentum scale (0.4), fit linearity (0.3), momentum resolution (0.2), radiative corrections (0.2), and beam energy uncertainty (0.1). Several of these are discussed further below.

When the spline fit is made to the baseline Monte Carlo sample, the shift, which should be exactly zero for an unbiased technique, is Δm=(+0.0±0.8) MeV, where the uncertainty from Monte Carlo statistics is retained as a systematic error on m_τ. The assumption that the shift in the spline is linear in mass with unit coefficient is tested by creating a second Monte Carlo sample, complete with full detector simulation, but with an input tau mass of 1784.0 MeV. This sample yields Δm=(+8.5±1.7) MeV, where again the error is from Monte Carlo statistics. A higher statistics test, but one with different systematics, is conducted by using simple smearing functions to simulate the detector response: a sample with tau mass input of 1772.0 MeV is fit to one generated with 1777.0 MeV, yielding a Δm=(−5.9±0.2) MeV. These tests of linearity allow the possibility that the coefficient of linearity is 5.9/5.0≃8.5/7.0≃1.2 instead of unity. Conversely, it is also possible that for smaller shifts the coefficient is unity but for larger shifts non-linear effects become noticeable. To account for both these possibilities, no correction is made for this effect but a systematic uncertainty in Δm of ±0.3 MeV is assigned.

To evaluate the accuracy of the momentum scale (p) in data and Monte Carlo samples, we examine both the momentum spectrum of the muons in $ee\rightarrow\mu\mu$ events and the reconstructed masses (m_D) of several charmed meson systems. The muon pair study gives $(\delta p/p)_{\mu\mu}$=(−1.0±0.5±3.2)×10^{-4}, where the largest contribution to the systematic error is due to uncertainty in the beam energy. The D channels analyzed (along with charge conjugates) are $D^0\rightarrow K^-\pi^+$, $D^0\rightarrow K^-\pi^+\pi^+\pi^-$, $D^+\rightarrow K^-\pi^+\pi^+$, and $D_s^0\rightarrow K^+K^+\pi^-$. The resulting limit on the accuracy of the momentum scale, averaged over the measured D modes, is $(\delta p/p)_D$=(−0.8±0.8±3.6)×10^{-4}, where the second error arises from uncertainty in the true D masses [5]. No dependence on charmed meson parent momentum, pseudoscalar decay product momenta, or data collection period is observed. Averaging $(\delta p/p)_{\mu\mu}$ and $(\delta p/p)_D$ yields an offset of $(\delta p/p)$=(−0.9±2.4)×10^{-4}. To convert the momentum scale offset and error to a corresponding offset and error in mass shift, the hadron momenta in the data are varied and new spline fits performed, yielding $\delta m/m$=1.04×$\delta p/p$. The mass shift offset and error to be applied to the data due to momentum scale is then (+0.2±0.4) MeV.

Differences between data and simulation in the momentum resolution could also affect the shape of the edge of the $(m_\tau)_{min}$ distribution near m_τ. The $\mu\mu$ final states and the four charmed hadron channels are again examined, this time focusing on the widths of the

reconstructed momentum and mass distributions, respectively. For the $\mu\mu$ (D) analysis, the data distributions are slightly narrower (wider) than the corresponding Monte Carlo simulation. As the two measures conflict on the sign of an effect, no offset to Δm is made, but a systematic error is assigned that includes the effect of the observed differences in resolution between data and Monte Carlo samples. The momenta of the hadrons in each data hh event are smeared with a Gaussian by an amount comparable to the discrepancy in the D's and muon pairs, and the $(m_\tau)_{min}$ plot again fit to find a mass shift. This procedure results in the assignment of a systematic uncertainty of ±0.2 MeV.

The effect of uncertain levels of non-tau backgrounds and tau-pair feed-across is evaluated by varying selection criteria, including those relevant for particle identification, over reasonable ranges. The observed changes lead to a ±0.7 MeV systematic error assignment.

Adding the net systematic offset and error to the spline fit result for Δm and the baseline mass yields m_τ=(1778.7$\pm$1.6$\pm$1.2) MeV for the hh analysis. This result can be combined with that of our published $h\rho$, $\rho\rho$ analysis, with which it is consistent. When common and independent errors are treated properly, the two results receive comparable weight and give a combined measurement of m_τ=(1778.2$\pm$0.8$\pm$1.0$\pm$0.7) MeV=(1778.2$\pm$1.4) MeV, where the three listed uncertainties are statistical, independent systematics, and correlated systematics, and have been combined in quadrature. Common sources of error include momentum scale, momentum resolution, beam energy, and radiative corrections.

The algebraic equation employed in this analysis for extracting m_τ involves the mass of the tau neutrino, m_{ν_τ}, which has heretofore been assumed to be zero. The fitted tau mass from this analysis can be expressed in terms of the neutrino mass and the true tau mass, for which we take m_τ^{BES} because it has no dependence on m_{ν_τ}, as

$$m_\tau^{FIT} \simeq m_\tau^{BES} - \frac{m_{\nu_\tau}^2}{m_0} \tag{10}$$

where m_0 is a mass parameter which adjusts the equation for several approximations. Using both the data and simulations, m_0 has been determined to be (1.6 $\pm$ 0.3) GeV. Eqn. 10 then yields $m_{\nu_\tau}^2$=(-1.9 ± 2.4)$\times10^3$ MeV^2. Taking the Bayesian approach [5] to limit the result to physical masses ($m_{\nu_\tau}^2 \geq 0$) gives $m_{\nu_\tau}<60$ MeV at 95% C.L.

VI. CONCLUSIONS

The CLEO branching fractions, tau mass, and tau lifetime [6] τ_τ=289$\pm$2.8$\pm$4.0 fs measurements can be inserted into Eqs. (1-3), yielding, respectively, the ratios of coupling constants

$$\frac{g_\mu}{g_e} = 1.0026 \pm 0.0055 \quad (\text{using } \mathcal{B}_\mu/\mathcal{B}_e) \tag{11}$$

$$\frac{g_\tau}{g_\mu} = 0.9999 \pm 0.0100 \quad (\text{using } \mathcal{B}_e, \ \tau_\tau, \ m_\tau) \tag{12}$$

$$\frac{g_\tau}{g_\mu} = 0.9972 \pm 0.0103 \quad (\text{using } \mathcal{B}_h, \ \tau_\tau, \ m_\tau) \tag{13}$$

each of which is consistent with unity, and hence with lepton universality. The μ-e universality ratio in Eq. (11) is about a factor of three less precise than that obtained from leptonic pion decay [28,29]. However, the tau decay result relates to the coupling of a transverse-W, whereas the pion decay test applies to longitudinal-W coupling [2–4]. The lifetime uncertainty dominates the error in both τ-μ universality measurements; they are almost completely correlated due to their similar dependence upon τ_τ, $N_{\tau\tau}$, and m_τ. Combining them yields g_τ/g_μ=0.9990±0.0098. If instead the world-average lifetime τ_τ=(291.0±1.5) fs [5] and mass m_τ=1777.00$^{+0.30}_{-0.27}$ [5] are used, we obtain g_τ/g_μ=0.9981±0.0056 using $\mathcal{B}_e$ and g_τ/g_μ=0.9948±0.0064 using $\mathcal{B}_h$, or, combining them, g_τ/g_μ=0.9970±0.0053. Here the branching fraction uncertainties dominate the errors.

The τ-μ universality test of Eq. (2) sometimes assumes μ-e universality, using a combined result $\mathcal{B}_\ell$ in place of $\mathcal{B}_e$, thereby improving the error due to branching fraction uncertainty. However, the weighted average of CLEO's $\mathcal{B}_e$ and $\mathcal{B}_\mu/0.9726$, $\mathcal{B}_\ell$=(17.79±0.18)%, differs insignificantly in precision from $\mathcal{B}_e$ because of strong correlations between the measurements.

The branching fractions and coupling-constant ratios measured here are consistent with and compare favorably in precision to other measurements [5]. In particular, the $\mathcal{B}_h$ and $\mathcal{B}_h/\mathcal{B}_e$ values presented here are the most precise published measurements, and are consistent with the prediction of Eq. (5), which is $\mathcal{B}_h/\mathcal{B}_e$=0.652±0.001 when the CLEO value of m_τ is used.

In summary, we have measured absolute branching fractions for $\tau \to e\nu\nu_\tau$, $\tau \to \mu\nu\nu_\tau$, $\tau \to h\nu_\tau$, and their ratios to one another, with relative errors of 1%. The tau mass has been measured with a relative error of 0.08%. The results show no indication for deviations from the Standard Model predictions. CLEO has measured the tau lifetime, mass, and $e/\mu/h$ branching fractions, providing all the ingredients for lepton universality tests in tau decay: μ-e and τ-μ universality are verified at the 0.5% and 1% levels, respectively.

ACKNOWLEDGMENTS

APPENDIX: LEPTON AND HADRON IDENTIFICATION PROBABILITIES

The lepton and hadron identification probabilities are measured in subsamples of the CLEO dataset with tracks which can be reliably tagged as leptons or non-leptons. Define $P(a{\to}b)$ to be the probability that particle species a (e, μ, or h) is identified as particle species b (e, μ, or h). Of the nine possible probabilities, two, $P(e{\to}\mu)$ and $P(\mu{\to}e)$, are trivially zero because the muon minimum momentum ($p_{\pm}{>}1.5$ GeV/c) and maximum calorimeter energy criteria ($E_{\pm}{<}0.6$ GeV) cannot be satisfied by a track which passes the electron requirement ($E_{\pm}/p_{\pm}{>}0.85$), and vice versa. Of the remaining seven probabilities, only four are independent: $P(e{\to}h){=}1-P(e{\to}e)$, $P(\mu{\to}h){=}1-P(\mu{\to}\mu)$, and $P(h{\to}h){=}1-P(h{\to}e)-P(h{\to}\mu)$. The probabilities $P(e{\to}e)$ and $P(\mu{\to}\mu)$ are the electron and muon "efficiencies"; $P(h{\to}e)$ and $P(h{\to}\mu)$ are commonly referred to as lepton "fake rates".

1. Efficiencies

Lepton efficiencies are determined from four different data samples with pairs of leptons detected in the final state: radiative Bhabhas ($ee{\to}ee\gamma$), radiative muon-pairs ($ee{\to}\mu\mu\gamma$), and the two-photon processes $ee{\to}eeee$ and $ee{\to}ee\mu\mu$. These samples are isolated primarily on the basis of kinematics, and hence the resulting efficiencies are minimally biased by the selection criteria. Each sample has a charged particle topology similar to the tau-pair events under investigation: two well-separated tracks in an event with little other detector activity. The efficiencies are tabulated in bins of momentum and polar angle.

The majority of $\ell\ell\gamma$ events have tracks of moderate to high momentum. To increase statistics, particularly at low momentum, di-lepton events with no other detected particles are also used for the efficiency calculation. These $\ell\ell X$ events originate as either $ee\ell\ell$ or $\ell\ell\gamma$ in which the scattered beam electrons or radiative photon escape detection at low angles to the beam. Such events are copiously produced and enhance the momentum spectrum at low ($ee\ell\ell$) and high ($\ell\ell\gamma$) momenta.

Radiative lepton events $\ell\ell\gamma$ are selected to have exactly two drift chamber tracks and one photon, defined as a calorimeter shower, not associated with a track, of energy $E_{\gamma}{>}0.1E_b$. The tracks and photon are required to be in the barrel region of the detector, $|\cos\theta_{\pm}|{<}0.707$. The tracks must have opposite charge, momenta $p_{\pm}{>}0.5$ GeV/c, acoplanarity $0.1{<}\xi{<}1.6$, and impact parameter $d_{\pm}{<}5$ mm. Calorimeter showers not associated with the tracks or photon candidate must sum to $E_{extra}{<}0.2$ GeV. To avoid overlap of track and photon calorimeter showers, which could bias the efficiency, the photon should be separated from the nearest shower associated with a track by space angle η. This separation must be larger for $ee\gamma$ events ($\eta{>}0.28$) than for $\mu\mu\gamma$ events ($\eta{>}0.17$) because electron showers spread laterally more than muon showers. Event kinematics are required to be loosely consistent with energy-momentum conservation: defining α as the space angle between the photon and the vector sum of the two track momenta, and $S_{tot}{=}(p_{+}{+}p_{-}{+}E_{\gamma})/E_b$ to be the total scaled visible energy, we require $\alpha{<}0.17$ and $1.75{<}S_{tot}{<}2.2$. Vector meson production and decay, $ee{\to}\gamma V$, $V{\to}\pi^+\pi^-$ is suppressed by the acoplanarity restriction for light states such as the ρ.

Further restrictions are imposed to isolate $ee\gamma$ and $\mu\mu\gamma$ event samples from each other. Radiative Bhabha events are not allowed to have any muon system hits matching projections

of charged tracks. The calorimeter energy $E_\pm$ associated with a track is required to satisfy $E_\pm > 0.3$ GeV for $ee\gamma$ and $E_\pm < 1.0$ GeV for $\mu\mu\gamma$. While these restrictions can, in principle, bias the resulting efficiencies, in practice any such effect is found to be negligible. To within 0.1%, electrons always have $E_\pm/p_\pm > 0.6$, and muons always deposit $E_\pm < 1.0$ GeV.

An $ee\ell\ell$ event will typically have two tracks nearly back-to-back in azimuth, non-zero net missing momentum p_{mis} that has polar angle $|\cos\theta_{mis}| \approx 1$, and no other detected particles. Hence, events with two tracks in the momentum and polar angle regions of interest ($|\cos\theta_\pm| < 0.707$ and $p_\pm > 0.5$ GeV/c) are selected for the $\ell\ell X$ sample if they have small acoplanarity ($\xi < 0.05$), substantially non-zero missing momentum ($p_{mis} > 0.1E_b$) pointing in the beam direction ($|\cos\theta_{mis}| > 0.99$), missing energy ($p_+ + p_- < 8$ GeV), and no significant calorimeter activity unassociated with the tracks ($E_{extra} < 0.1$ GeV). For the eeX sample $E_\pm/p_\pm > 0.5$ is required for both tracks, which effectively eliminates non-electron backgrounds. Harsher criteria for the $\mu\mu X$ sample are necessary to eliminate cosmic rays and other two-photon processes. Cosmic rays are suppressed to below the 0.1% level by tightening the acoplanarity restriction to $\xi < 0.01$, and by imposing new requirements: the track impact parameters must satisfy $d_\pm < 1$ mm, the acollinearity of the two tracks in three dimensions must exceed 0.1, the position on each track closest to the IP along the beam direction must satisfy $z_\pm < 40$ mm, and, if available, the time-of-flight scintillation counters must yield times consistent, within 1 ns, with an event originating at the IP. The two-photon process $ee \to eehh$ is suppressed in the $\mu\mu X$ sample to below 0.1% by requiring each muon to have calorimeter energy deposition $E_\pm < 1$ GeV and the invariant mass of the two-track system to satisfy $W > 3$ GeV [26,27].

About 240k $ee\gamma$, 40k $\mu\mu\gamma$, 250k eeX, and 30k $\mu\mu X$ events constitute the tagged lepton samples for efficiency measurements. The momentum spectra for the tracks in these events are shown in Fig. 11. The peaks at large momenta in the $\ell\ell X$ samples correspond to $\ell\ell\gamma$ in which the radiated photon has been emitted nearly parallel to the beam and hence is undetected. The $\ell\ell X$ samples significantly enhance statistics below 2.5 GeV/c, particularly for electrons. The enhancement is not as great for muons primarily because of the $W > 3$ GeV requirement.

Events from $\ell\ell X$ and $\ell\ell\gamma$ samples are combined for the final efficiencies shown in Fig. 12 for electrons and Fig. 13 for muons, both binned in momentum and $|\cos\theta_\pm|$. Momentum and polar angle bin sizes are chosen to adequately represent the efficiency variations in these variables. For electrons, $P(e \to e) \approx 98\%$, and shows only modest momentum and polar angle dependence. The efficiency drop-off at low momentum near $|\cos\theta_\pm| = 0.7$ is due to the energy loss that the electron experiences as it traverses support material near the outer radius of the main drift chamber endplate. For muons, the $P(\mu \to \mu) \approx 93\%$ efficiency also declines at low momentum for large $|\cos\theta_\pm|$; at increasingly non-normal incidence to the magnet iron, lower momentum muons have difficulty penetrating more absorber. The separate efficiencies from $\ell\ell\gamma$ and $\ell\ell X$ are everywhere statistically consistent with each other.

In the $ee\gamma$ and eeX samples, there are no signs in the $E_\pm/p_\pm$ distributions of hadronic background, which would fall with increasing $E_\pm/p_\pm$. Fig. 14 shows $E_\pm/p_\pm$ for tracks from the $ee\gamma$ sample in two momentum bins. Distributions in all momentum bins, including those shown, are well-behaved for $E_\pm/p_\pm = 0.5$-0.7, showing no sign of significant hadronic contamination. These plots also verify that negligible bias is introduced by the requirements $E_\pm > 0.3$ GeV for $ee\gamma$ and $E_\pm/p_\pm > 0.5$ for eeX. The $E_\pm$ distributions for $\mu\mu\gamma$ and $\mu\mu X$

events, shown for two momentum bins in Fig. 15, also exhibit no indication of hadronic background, which would show up as enhancements for $E_\pm > 0.4$ GeV. These distributions verify negligible bias from the $E_\pm < 1.0$ GeV cut on $\mu\mu\gamma$ and $\mu\mu X$ events.

When the binned lepton identification probabilities from Figs. 12 and 13 are applied to the lepton momentum and angular distributions expected from tau decay, the error from efficiency statistics on the integrated lepton efficiency is 0.03% for electrons and 0.12% for muons. Systematic errors on (e, μ) probabilities comprise potential effects from biased event selection (0.05%, 0.10%), backgrounds (0.05%, 0.10%), and variations of the efficiencies with momentum, polar and azimuthal angle, charge, and time inside the bins of momentum and polar angle (0.12%, 0.24%). Thus, for leptons from tau decay, the total error from statistics and systematics combined in quadrature is estimated to be $\pm 0.15\%$ for electrons and $\pm 0.30\%$ for muons.

2. Fake rates

The hadron-faking-lepton probabilities $P(h \rightarrow e)$ and $P(h \rightarrow \mu)$ are determined from a sample of tracks with a lepton recoiling against an $h\pi^0$ system $(l - h\pi^0)$. The selection criteria are similar to but looser than those for ρe and $\rho \mu$ events described in Section III: the leptons are identified as e or μ, and the opposite track "tagged" by requiring a nearby reconstructed π^0 (without regard to its identity as a lepton). To obtain more statistics, the minimum scaled energy for the higher energy photon in the π^0 is relaxed from $x_\gamma > 0.2$ to $x_\gamma > 0.015$. Some care has been taken to suppress multi-π^0 events in which a photon could overlap the hadron calorimeter shower, boosting its $E_\pm/p_\pm$ above that for a single pion or kaon: $E_\pm/p_\pm < 1.1$ for the h is required, and showers not associated with the two charged tracks or the π^0 must have energy $E_\gamma < 0.05$ GeV. Fakes are then obtained by applying the lepton identification criteria to the hadronic track.

Events with two leptons and a fake π^0 in this sample could potentially bias the fake probabilities. However, radiative lepton-pairs are heavily suppressed by the selection criteria, and remaining small fake-π^0 backgrounds (about 2% of the sample) are explicitly removed with a π^0-sideband subtraction of the probabilities. The μ-tag and e-tag samples have statistically compatible fake rates after this subtraction, yielding no indication of any residual lepton contamination in the hadron sample.

The two identification criteria for electrons, $E_\pm/p_\pm$ and dE/dx, are independent. Therefore the probability for a hadron to pass each requirement separately is measured, and the two resulting probabilities multiplied together for each momentum bin. Since the $P(h \rightarrow e)$ probabilities are small, this procedure efficiently utilizes the limited statistics available in the $l - h\pi^0$ sample.

The resulting faking probabilities are shown, with statistical errors only, in Fig. 16 for electrons and Fig. 17 for muons, as a function of hadron charge and momentum. Hadrons fake electrons and muons with probabilities 0.1-0.5% and 1-5%, respectively, depending upon charge and momentum. The muon fake rate is much higher for $p_\pm = 1.5$-2.0 GeV/c because, in order to keep the muon detection efficiency $P(\mu \rightarrow \mu)$ approximately constant, the number of interaction lengths required for muon identification steps down from five to three in that bin. Positive hadrons fake electrons much more often than negative below 2.5 GeV/c due to

21

a higher probability for positive hadrons to shower in the cesium iodide and thereby satisfy the $E_\pm/p_\pm$ criterion.

Systematic effects can arise from QED and tau backgrounds, variations of rate with angle, and π/K content relative to that of fake leptons in the signal samples. Non-π^0 tau and non-tau backgrounds are explicitly subtracted; multi-π^0 effects are estimated from Monte Carlo studies of tau events to increase the measured $P(h{\to}e)$ fake rate by only 2.5% (relative) and are ignored. The fake probabilities are nearly constant in polar angle. Studies of tagged kaons from D^0 decays show that kaons fake leptons at a somewhat different rate than pions. However, Monte Carlo studies indicate that the hadrons in the $l-h\pi^0$ sample consist of 2% kaons, close to the kaon fraction of fake leptons in the signal samples. Hence the π/K mix is a negligible effect. The relative error on the fake probabilities, from statistics and systematics combined in quadrature and integrated over momentum, is estimated to be $\pm15\%$ for both $P(h{\to}e)$ and $P(h{\to}\mu)$.

REFERENCES

[1] W.J. Marciano and A. Sirlin, Phys. Rev. Lett. **61**, 1815 (1988).

[2] R. Decker and M. Finkemeier, Phys. Lett. B **334**, 199 (1994) and Nucl. Phys. **B438**, 17 (1995).

[3] W.J. Marciano and A. Sirlin, Phys. Rev. Lett. **71**, 3629 (1993).

[4] W.J. Marciano, in *Tau 94*, Proceedings of the Third Workshop on Tau Lepton Physics, Montreux, Switzerland, 1994, edited by L. Rolandi, [Nucl. Phys. B (Proc. Suppl.) **40**, 3 (1995)].

[5] Particle Data Group, R.M. Barnett *et al.*, Phys. Rev. D **54**, 1 (1996).

[6] CLEO Collaboration, R. Balest *et al.*, Phys. Lett. B **388**, 402 (1996).

[7] CLEO Collaboration, R. Balest *et al.*, Phys. Rev. D **47**, R3671 (1993).

[8] CLEO Collaboration, Y. Kubota *et al.*, Nucl. Instrum. Methods Phys. Res., Sect. A **320**, 66 (1992).

[9] The CLEO coordinate system has x pointing radially outward from the center of the CESR ring, y upward, and z along the positron direction. The polar angle θ is measured with respect to the $z-$axis, and azimuth ϕ in the $x-y$ plane with respect to the $x-$axis.

[10] C. Bebek *et al.*, Nucl. Instrum. Methods Phys. Res., Sect. A **302**, 261 (1991).

[11] CLEO Collaboration, M. Artuso *et al.*, Phys. Rev. Lett. **72**, 3762 (1994).

[12] CLEO Collaboration, G. Crawford *et al.*, Nucl. Instrum. Methods Phys. Res., Sect. A **345**, 429 (1994).

[13] KORALB (v.2.2) / TAUOLA (v.2.4): S. Jadach and Z. Was, Comput. Phys. Commun. **36**, 191 (1985); **64**, 267 (1991); S. Jadach, J.H. Kühn, and Z. Was, *ibid.* **64**, 275 (1991); **70**, 69 (1992), **76**, 361 (1993).

[14] R. Brun *et al.*, GEANT v. 3.15, CERN DD/EE/84-1 (unpublished).

[15] Tau branching fractions with K_L^0's assumed for this analysis are 0.44% for $\tau \to K_L^0 \pi \nu_\tau$, 0.05% for $K_L^0 K \nu_\tau$, 0.28% for $K_L^0 \pi \pi^0 \nu_\tau$, and 0.07% for $K_L^0 K \pi^0 \nu_\tau$.

[16] J. Vermasseren, Nucl. Phys. **B229**, 347 (1983).

[17] V.M. Budnev *et al.*, Phys. Rep. **15**, 181 (1975).

[18] F. Berends and R. Kleiss, Nucl. Phys. **B228**, 537 (1983).

[19] BHLUMI v. 1.22: S. Jadach, E. Richter-Was, B.F.L. Ward, and Z. Was, CERN-TH-6230-91 (Sept. 1991); Phys. Lett. B **268**, 253 (1991); **260**, 438 (1991); **253**, 469 (1991); S. Jadach and B.F.L. Ward, Phys. Rev. D **40**, 3582 (1989).

[20] R. Kleiss and S. van der Marck, Nucl. Phys. **B342**, 61 (1990).

[21] CLEO Collaboration, D.S. Akerib *et al.*, Phys. Rev. Lett. **69**, 3610 (1992); **71**, 3395(E) (1993).

[22] CLEO Collaboration, R. Ammar *et al.*, Phys. Rev. D **45**, 3976 (1992).

[23] BES Collaboration, J.Z. Bai *et al.*, Phys. Rev. D **53**, 20 (1996).

[24] ARGUS Collaboration, H. Albrecht, *et al.*, Phy. Lett. B **292**, 221 (1992).

[25] J. Mevissen, Ph.D. Thesis, Cornell University, 1996.

[26] D. Acosta, Ph.D. Thesis, Univ. of California at San Diego, 1993.

[27] CLEO Collaboration, J. Dominick *et al.*, Phys. Rev. D **50**, 3027 (1994).

[28] D. Britton *et al.*, Phys. Rev. Lett. **68**, 3000 (1992).

[29] C. Czapek *et al.*, Phys. Rev. Lett. **70**, 17 (1993).

TABLE I. Product branching fractions and their components for each tau-pair decay mode.

ab	n	$\mathcal{A}(\%)$	$\mathcal{P}(\%)$	$\mathcal{T}(\%)$	$f(\%)$	$\mathcal{B}_a \times \mathcal{B}_b \ (10^{-2})$
ee	11019	11.304±0.123	95.59±0.30	97.51±0.52	1.62±0.48	3.166±0.030±0.062
$\mu\mu$	3846	5.443±0.060	86.01±0.57	79.00±1.23	4.10±0.63	3.069±0.049±0.078
hh	4970	9.900±0.129	95.29±0.65	86.20±0.93	27.68±0.87	1.360±0.019±0.035
$e\mu$	17364	9.706±0.104	90.75±0.33	96.29±0.63	2.38±0.38	3.075±0.023±0.060
eh	14880	10.102±0.109	95.45±0.36	97.03±0.66	17.43±0.68	2.021±0.017±0.043
μh	9739	7.868±0.090	90.62±0.43	83.60±1.00	20.01±1.12	2.011±0.020±0.053
ρe	15314	3.909±0.043	96.42±0.25	97.35±0.63	1.68±0.12	6.313±0.051±0.122
$\rho\mu$	11505	3.148±0.035	91.69±0.35	97.44±0.66	3.09±0.28	6.099±0.057±0.121
ρh	9846	3.259±0.038	96.34±0.46	97.51±0.71	18.28±0.52	4.043±0.041±0.086

TABLE II. Trigger efficiency components (%) for each tau-pair decay mode.

ab	TF-ctr	TF-edge	Crystal	Track	L3
ee	99.70±0.15	99.44±0.40	99.80±0.15	98.55±0.28	100
$e\mu$	99.70±0.15	99.04±0.32	99.80±0.15	98.30±0.48	99.40±0.18
eh	99.70±0.15	99.71±0.38	99.80±0.15	98.30±0.48	99.49±0.18
ρe	99.70±0.15	99.53±0.36	99.80±0.15	98.30±0.48	100
$\rho\mu$	99.70±0.15	99.83±0.41	99.80±0.15	98.18±0.48	99.92±0.08
ρh	99.70±0.15	99.82±0.49	99.80±0.15	98.18±0.48	100
$\mu\mu$	−	−	89.05±0.80	93.32±0.48	95.06±1.10
μh	−	−	92.10±0.87	93.32±0.48	97.27±0.52
hh	−	−	93.62±0.75	93.32±0.48	98.66±0.51

TABLE III. Background fractions f (%) by source for each tau-pair decay mode. Relative systematic uncertainties for $ee\tau\tau$, $\ell\ell$, and $ee\ell\ell$ entries are 100%. Here $\ell\ell \equiv ee$ or $\mu\mu$.

ab	$\tau\tau$	Cosmic	$ee\tau\tau$	$\ell\ell$	$ee\ell\ell$
ee	0.83±0.13	−	0.24	0.32	0.23
$\mu\mu$	3.62±0.58	0.15±0.07	0.11	0.22	−
hh	27.16±0.81	0.10±0.05	0.29	0.06	0.07
$e\mu$	2.13±0.34	−	0.12	−	0.13
eh	16.78±0.50	−	0.32	−	0.33
μh	18.51±0.56	0.13±0.07	0.12	0.34	0.90
ρe	1.57±0.06	−	0.10	−	0.01
$\rho\mu$	3.09±0.28	−	−	−	−
ρh	18.08±0.49	0.01±0.01	0.16	−	0.03

TABLE IV. Tau-Pair feed-across (%) into each selected tau-pair decay mode, listed by true Monte Carlo tau decay mode (neutrinos omitted).

ab	e	μ	h	$h\pi^0$	$h{\geq}2\pi^0$	$K_L^0 h$	$K_L^0 h\pi^0$	Other
ee	—	—	0.78	0.04	—	0.01	—	—
$\mu\mu$	—	—	3.37	0.18	0.01	0.06	—	—
hh	4.25	14.36	—	6.12	0.10	2.12	0.15	0.06
$e\mu$	—	—	1.98	0.11	0.01	0.03	—	—
eh	2.58	9.02	0.36	3.61	0.04	1.03	0.10	0.04
μh	2.62	9.14	1.83	3.71	0.08	1.02	0.09	0.02
ρe	—	—	0.32	0.03	—	0.10	0.78	0.34
$\rho\mu$	—	—	1.76	0.08	0.01	0.13	0.75	0.36
ρh	2.60	8.96	0.10	3.81	0.10	1.16	0.87	0.48

TABLE V. Fit result for $\mathcal{B}_e$, with six independent product branching fraction combinations ordered by their weights in the fit.

Method	$\mathcal{B}_e$ (%)	Wt
$\sqrt{\mathcal{B}_e\mathcal{B}_e}$	17.79±0.08±0.17	0.66
$\sqrt{\mathcal{B}_e\mathcal{B}_\mu \cdot \mathcal{B}_\rho\mathcal{B}_e/\mathcal{B}_\rho\mathcal{B}_\mu}$	17.84±0.13±0.23	0.14
$\sqrt{\mathcal{B}_e\mathcal{B}_h \cdot \mathcal{B}_\rho\mathcal{B}_e/\mathcal{B}_\rho\mathcal{B}_h}$	17.76±0.14±0.25	0.09
$\mathcal{B}_e\mathcal{B}_\mu/\sqrt{\mathcal{B}_\mu\mathcal{B}_\mu}$	17.55±0.19±0.29	0.04
$\mathcal{B}_e\mathcal{B}_h/\sqrt{\mathcal{B}_h\mathcal{B}_h}$	17.33±0.19±0.32	0.04
$\sqrt{\mathcal{B}_e\mathcal{B}_\mu \cdot \mathcal{B}_e\mathcal{B}_h/\mathcal{B}_\mu\mathcal{B}_h}$	17.58±0.13±0.28	0.03
Fit: χ^2=2.8/5 dof	17.76±0.06±0.17	-

TABLE VI. Fit result for $\mathcal{B}_\mu$, with six independent product branching fraction combinations ordered by their weights in the fit.

Method	$\mathcal{B}_\mu$ (%)	Wt
$\sqrt{\mathcal{B}_\mu \mathcal{B}_\mu}$	$17.52\pm0.14\pm0.22$	0.35
$\sqrt{\mathcal{B}_e \mathcal{B}_\mu \cdot \mathcal{B}_\rho \mathcal{B}_\mu / \mathcal{B}_\rho \mathcal{B}_e}$	$17.24\pm0.12\pm0.21$	0.34
$\mathcal{B}_e \mathcal{B}_\mu / \sqrt{\mathcal{B}_e \mathcal{B}_e}$	$17.28\pm0.15\pm0.26$	0.14
$\sqrt{\mathcal{B}_\mu \mathcal{B}_h \cdot \mathcal{B}_\rho \mathcal{B}_\mu / \mathcal{B}_\rho \mathcal{B}_h}$	$17.42\pm0.15\pm0.27$	0.11
$\sqrt{\mathcal{B}_e \mathcal{B}_\mu \cdot \mathcal{B}_\mu \mathcal{B}_h / \mathcal{B}_e \mathcal{B}_h}$	$17.49\pm0.13\pm0.27$	0.04
$\mathcal{B}_\mu \mathcal{B}_h / \sqrt{\mathcal{B}_h \mathcal{B}_h}$	$17.24\pm0.21\pm0.39$	0.02
Fit: $\chi^2 = 2.8/5$ dof	$17.37\pm0.08\pm0.18$	-

TABLE VII. Fit result for $\mathcal{B}_h$, with six independent product branching fraction combinations ordered by their weights in the fit.

Method	$\mathcal{B}_h$ (%)	Wt
$\sqrt{\mathcal{B}_h \mathcal{B}_h}$	$11.66\pm0.08\pm0.15$	0.42
$\sqrt{\mathcal{B}_e \mathcal{B}_h \cdot \mathcal{B}_\rho \mathcal{B}_h / \mathcal{B}_\rho \mathcal{B}_e}$	$11.38\pm0.09\pm0.15$	0.29
$\sqrt{\mathcal{B}_\mu \mathcal{B}_h \cdot \mathcal{B}_\rho \mathcal{B}_h / \mathcal{B}_\rho \mathcal{B}_\mu}$	$11.55\pm0.10\pm0.18$	0.12
$\mathcal{B}_e \mathcal{B}_h / \sqrt{\mathcal{B}_e \mathcal{B}_e}$	$11.36\pm0.11\pm0.19$	0.11
$\sqrt{\mathcal{B}_e \mathcal{B}_h \cdot \mathcal{B}_\mu \mathcal{B}_h / \mathcal{B}_e \mathcal{B}_\mu}$	$11.50\pm0.09\pm0.18$	0.04
$\mathcal{B}_\mu \mathcal{B}_h / \sqrt{\mathcal{B}_\mu \mathcal{B}_\mu}$	$11.48\pm0.15\pm0.26$	0.02
Fit: $\chi^2 = 2.8/5$ dof	$11.52\pm0.05\pm0.12$	-

TABLE VIII. Fit result for $\mathcal{B}_\mu/\mathcal{B}_e$, with six independent product branching fraction combinations ordered by their weights in the fit.

Method	$\mathcal{B}_\mu/\mathcal{B}_e$ (%)	Wt
$\sqrt{\mathcal{B}_\mu\mathcal{B}_\mu/\mathcal{B}_e\mathcal{B}_e}$	98.46±0.92±1.13	0.39
$\mathcal{B}_\rho\mathcal{B}_\mu/\mathcal{B}_\rho\mathcal{B}_e$	96.61±1.19±1.53	0.29
$\mathcal{B}_e\mathcal{B}_\mu/\mathcal{B}_e\mathcal{B}_e$	97.13±1.18±1.53	0.21
$\mathcal{B}_\mu\mathcal{B}_h/\mathcal{B}_e\mathcal{B}_h$	99.51±1.30±2.47	0.11
$(\mathcal{B}_e\mathcal{B}_\mu \cdot \mathcal{B}_\rho\mathcal{B}_h)/(\mathcal{B}_e\mathcal{B}_h \cdot \mathcal{B}_\rho\mathcal{B}_e)$	97.44±1.66±2.28	<0.01
$(\mathcal{B}_\mu\mathcal{B}_h \cdot \mathcal{B}_\rho\mathcal{B}_h)/(\mathcal{B}_\rho\mathcal{B}_e \cdot \mathcal{B}_h\mathcal{B}_h)$	94.70±2.05±2.91	<0.01
Fit: χ^2=2.8/5 dof	97.77±0.63±0.87	-

TABLE IX. Fit result for $\mathcal{B}_h/\mathcal{B}_e$, with six independent product branching fraction combinations ordered by their weights in the fit.

Method	$\mathcal{B}_h/\mathcal{B}_e$ (%)	Wt
$\sqrt{\mathcal{B}_h\mathcal{B}_h/\mathcal{B}_e\mathcal{B}_e}$	65.54±0.56±0.77	0.43
$\mathcal{B}_\rho\mathcal{B}_h/\mathcal{B}_\rho\mathcal{B}_e$	64.04±0.83±1.11	0.25
$\mathcal{B}_e\mathcal{B}_h/\mathcal{B}_e\mathcal{B}_e$	63.83±0.80±1.12	0.17
$\mathcal{B}_\mu\mathcal{B}_h/\mathcal{B}_e\mathcal{B}_\mu$	65.40±0.83±1.54	0.13
$\mathcal{B}_e\mathcal{B}_h \cdot \mathcal{B}_\rho\mathcal{B}_\mu/\mathcal{B}_e\mathcal{B}_\mu \cdot \mathcal{B}_\rho\mathcal{B}_e$	63.50±1.06±1.42	0.02
$\mathcal{B}_\mu\mathcal{B}_h \cdot \mathcal{B}_\rho\mathcal{B}_\mu/\mathcal{B}_\rho\mathcal{B}_e \cdot \mathcal{B}_\mu\mathcal{B}_\mu$	63.31±1.44±1.85	<0.01
Fit: χ^2=2.8/5 dof	64.84±0.41±0.60	-

TABLE X. Mode sensitivity of the branching fraction errors from studies using the simultaneous global fit. Relative increase (%) of the absolute error for each branching fraction when a single mode is omitted.

Mode	$\mathcal{B}_e$	$\mathcal{B}_\mu$	$\mathcal{B}_h$	$\mathcal{B}_\mu/\mathcal{B}_e$	$\mathcal{B}_h/\mathcal{B}_e$
ee	28.6	0.9	0.7	35.6	31.4
$\mu\mu$	0.2	13.8	0.1	18.3	0.1
hh	0.1	0.1	13.3	<0.1	16.5
$e\mu$	2.4	8.9	0.1	2.7	2.8
eh	1.6	0.1	9.7	2.0	4.3
μh	0.1	1.9	2.3	2.9	3.4
ρe	2.6	3.2	2.8	11.8	10.4
$\rho\mu$	0.8	5.6	0.7	11.4	<0.1
ρh	0.5	0.5	6.9	<0.1	11.4

TABLE XI. Relative errors (%) by source.

Source	$\mathcal{B}_e$	$\mathcal{B}_\mu$	$\mathcal{B}_h$	$\mathcal{B}_\mu/\mathcal{B}_e$	$\mathcal{B}_h/\mathcal{B}_e$
Statistics (n)	0.36	0.47	0.46	0.65	0.63
Normalization ($N_{\tau\tau}$)	0.71	0.71	0.71	-	-
Acceptance ($\mathcal{A}$)	0.48	0.54	0.54	0.56	0.56
Trigger ($\mathcal{T}$)	0.28	0.40	0.37	0.51	0.48
Background (f)	0.19	0.23	0.39	0.32	0.43
Particle Id ($\mathcal{P}$)	0.16	0.32	0.31	0.36	0.34
Quadrature Sum	1.00	1.15	1.18	1.10	1.12

TABLE XII. Correlation coefficients between branching fraction measurements.

	$\mathcal{B}_\mu$	$\mathcal{B}_h$	$\mathcal{B}_\mu/\mathcal{B}_e$	$\mathcal{B}_h/\mathcal{B}_e$
$\mathcal{B}_e$	0.75	0.71	0.48	0.46
$\mathcal{B}_\mu$		0.64	0.62	0.30
$\mathcal{B}_h$			0.28	0.64
$\mathcal{B}_\mu/\mathcal{B}_e$				0.59

2541096-008
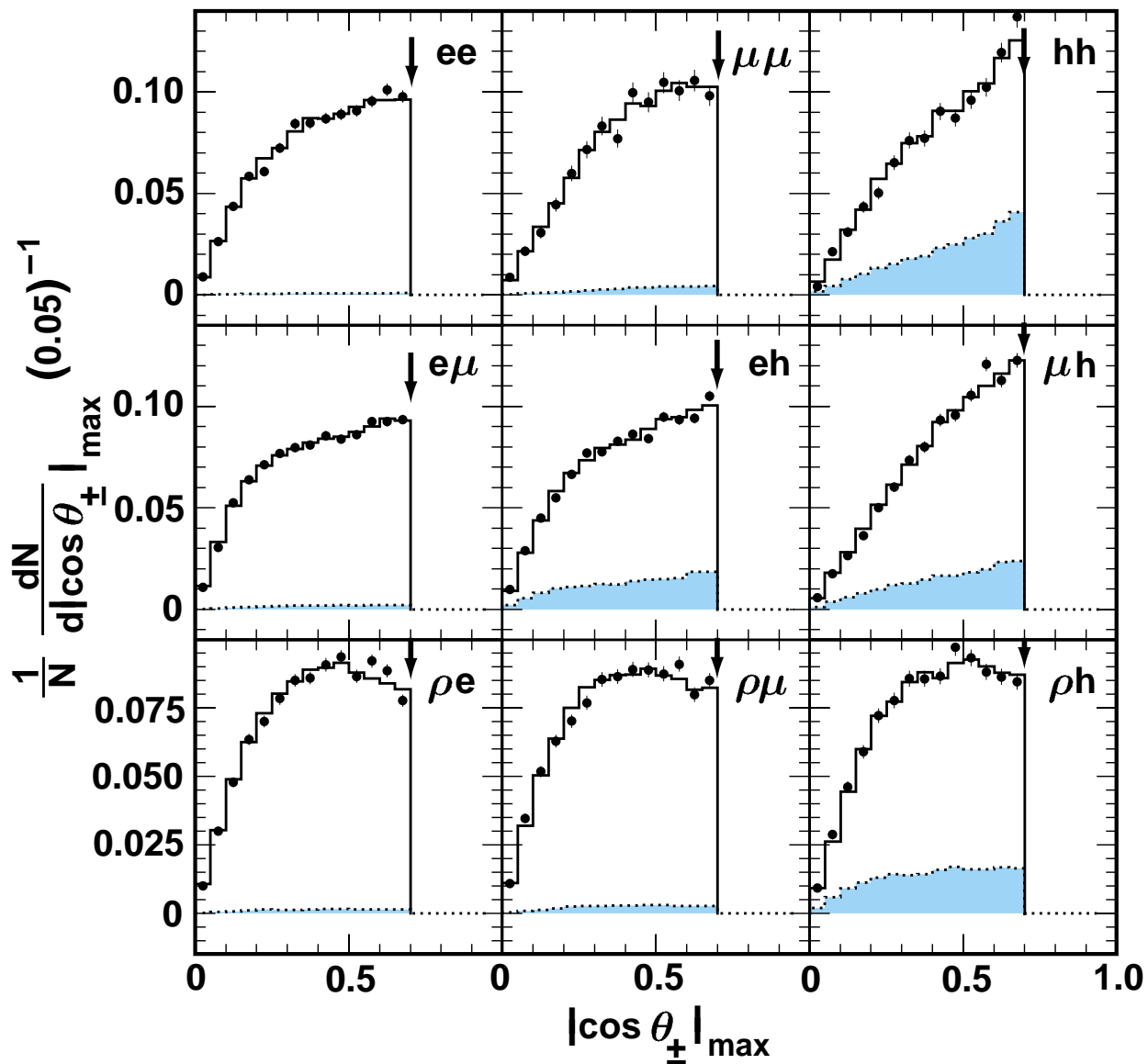
FIG. 1. Distributions in $|\cos\theta_{\pm}|_{max}$ for data with statistical errors (solid circles with error bars) and Monte Carlo simulation (histogram) for the nine indicated tau-pair decay modes. The lightly shaded area represents the contributions from tau-pair feed-across. Vertical arrows indicate cut values on this variable.
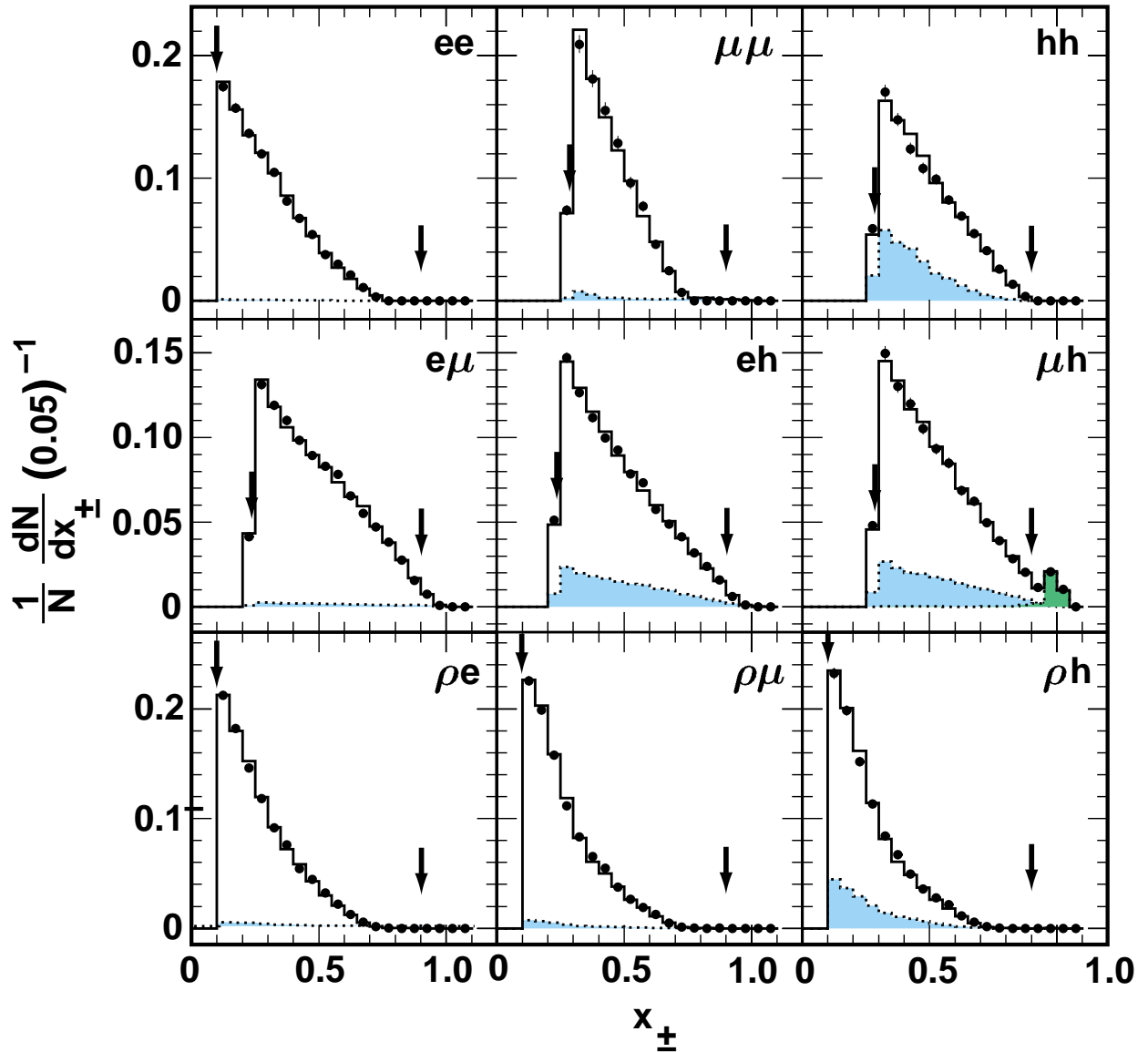
FIG. 2. Distributions in $x_{\pm}$, with symbols defined as in Fig. 1. The lower momentum track is plotted for ee, $\mu\mu$, and hh, the electron's for $e\mu$ and eh, the muon's for μh, and the ρ's charged track's for the ρ-tag modes. The darkly shaded region in the μh plot at high momentum indicates the Monte Carlo prediction for $ee \rightarrow \mu\mu$ background.
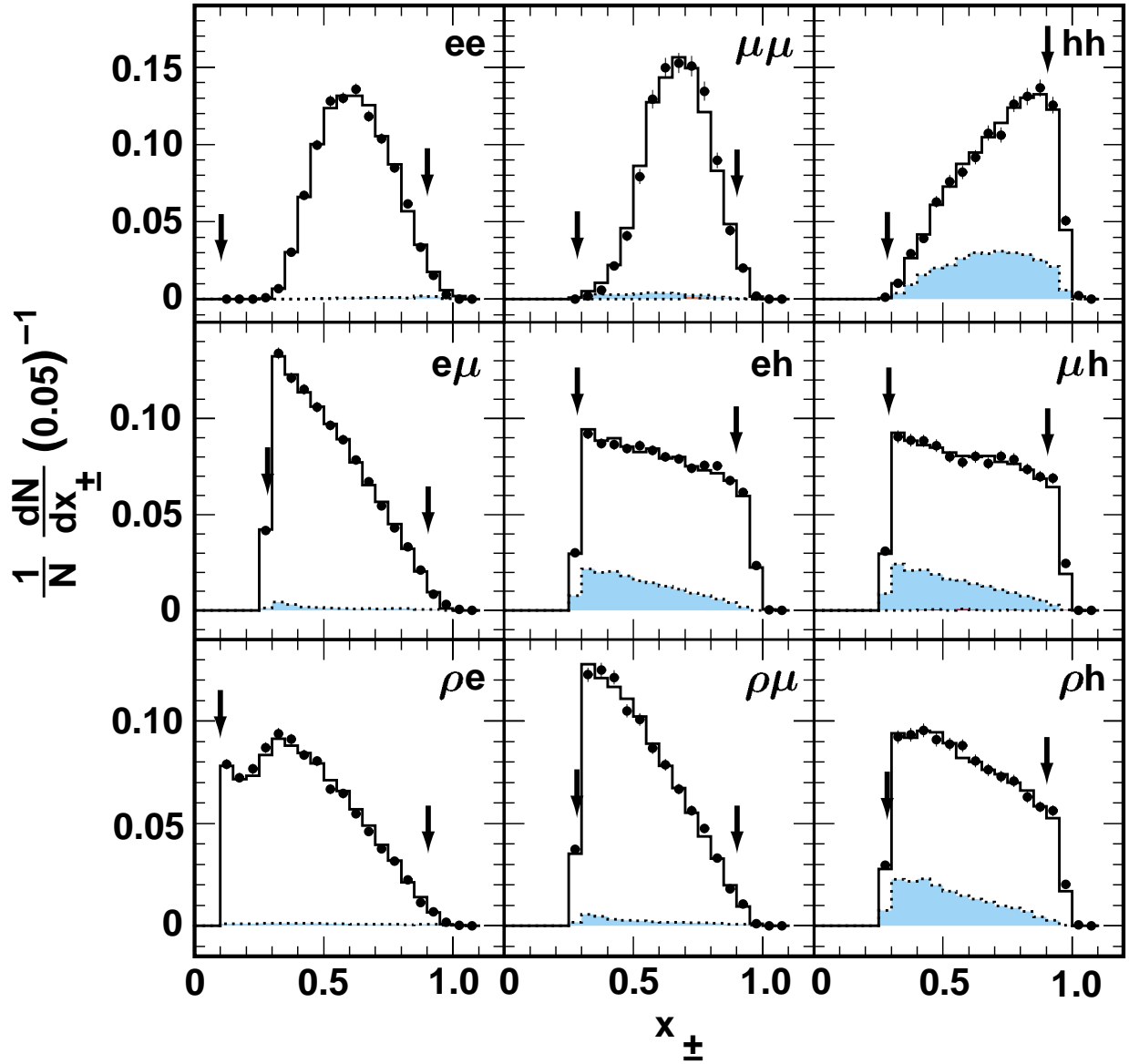
FIG. 3. Distributions in $x_\pm$, with symbols defined as in Fig. 1. The higher momentum track is plotted for ee, $\mu\mu$, and hh, the muon's for $e\mu$, the hadron's for eh and μh, and the track's opposite the ρ for the ρ-tag modes.
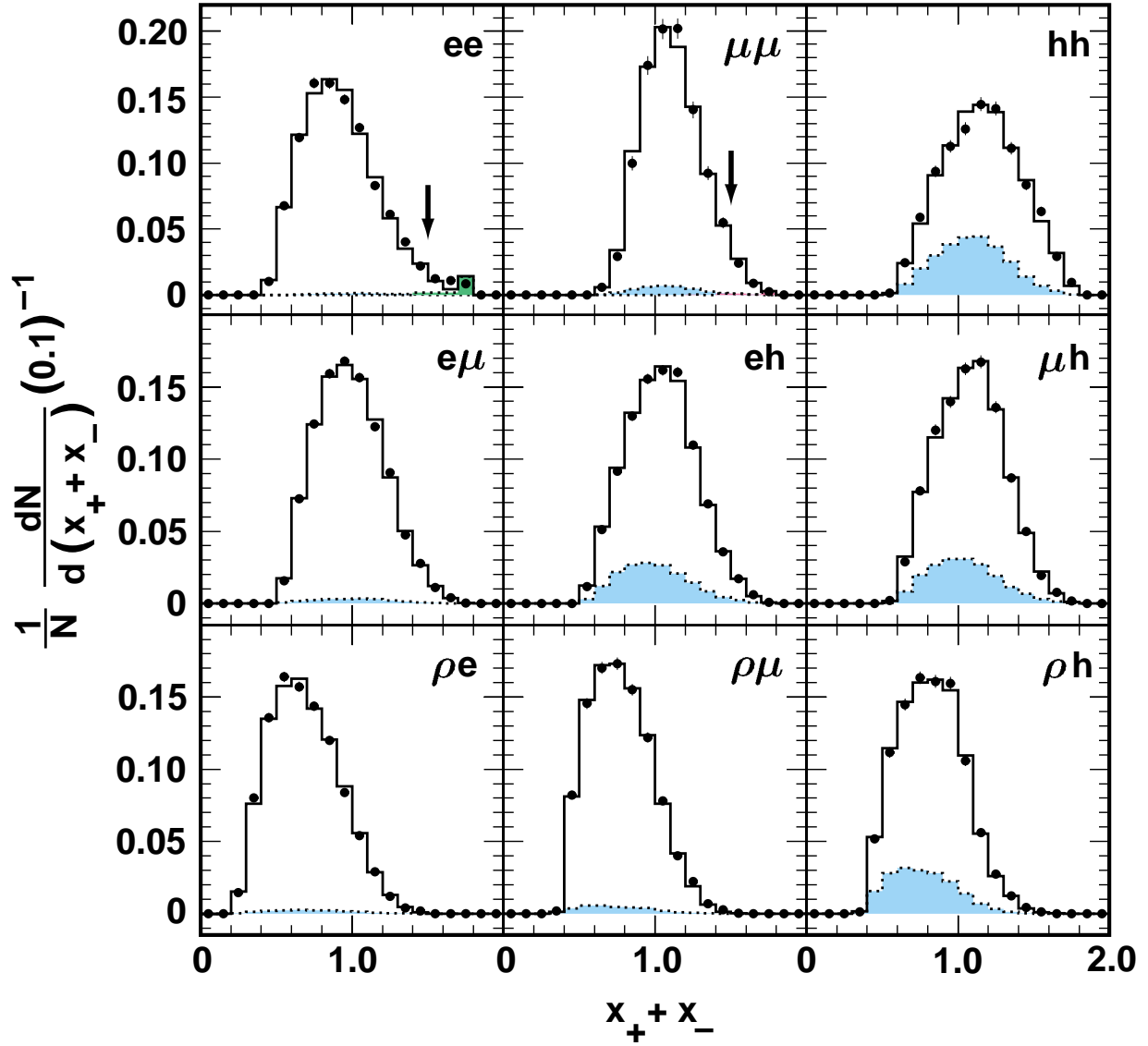
FIG. 4. Distributions in $(x_+ + x_-)$, with symbols defined as in Fig. 1. The darkly shaded regions in the ee and $\mu\mu$ plots at high $(x_+ + x_-)$ indicate the Monte Carlo predictions for $ee{\rightarrow}ee$ and $ee{\rightarrow}\mu\mu$ background.
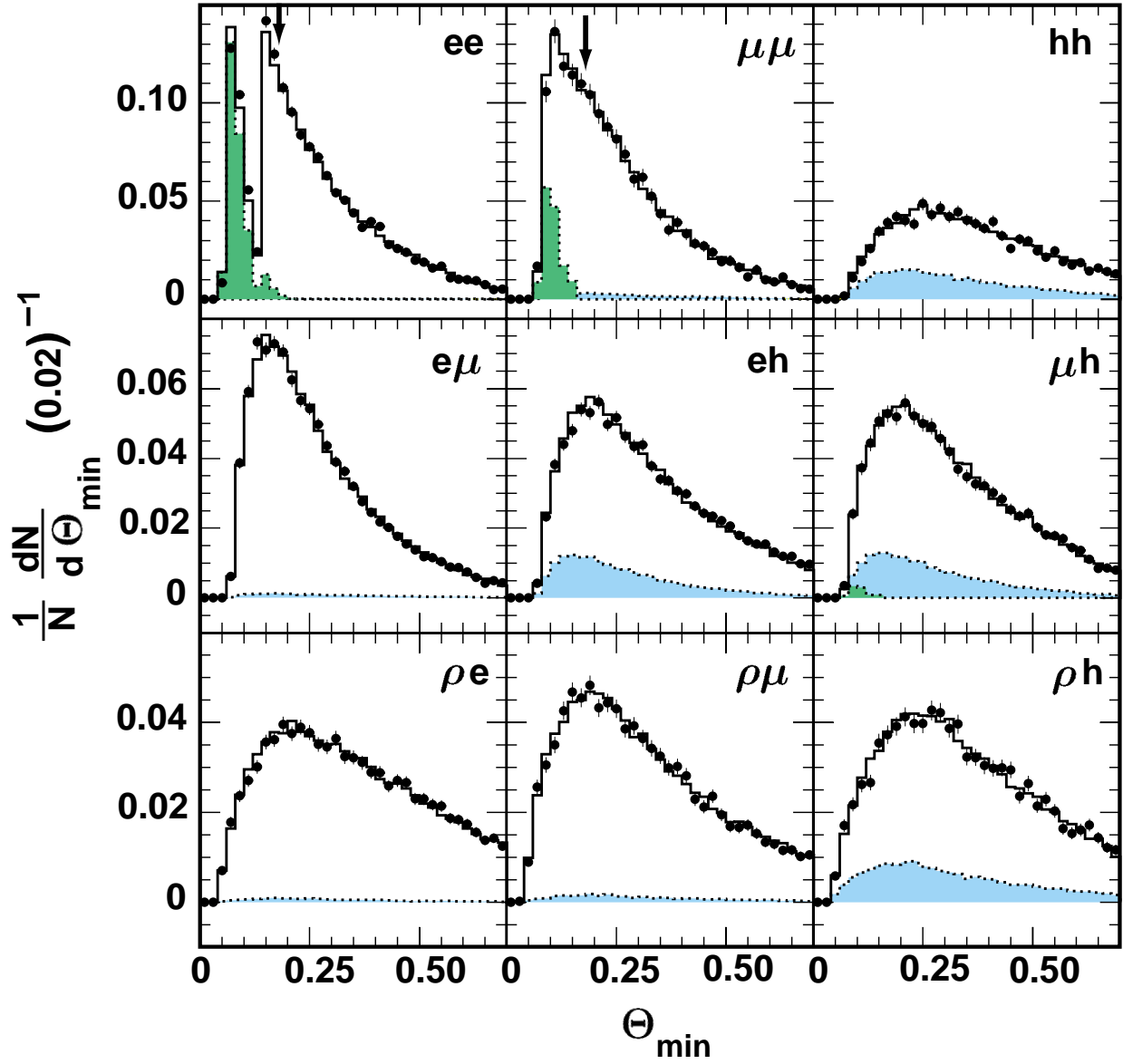
FIG. 5. Distributions in $\Theta_{\min}$, with symbols defined as in Fig. 1. The darkly shaded regions in the ee and $\mu\mu$ plots at small $\Theta_{\min}$ indicate the Monte Carlo predictions for $ee\rightarrow eeee$ and $ee\rightarrow ee\mu\mu$ backgrounds, respectively. The first 7 bins in the ee plot are scaled down by a factor of 8.
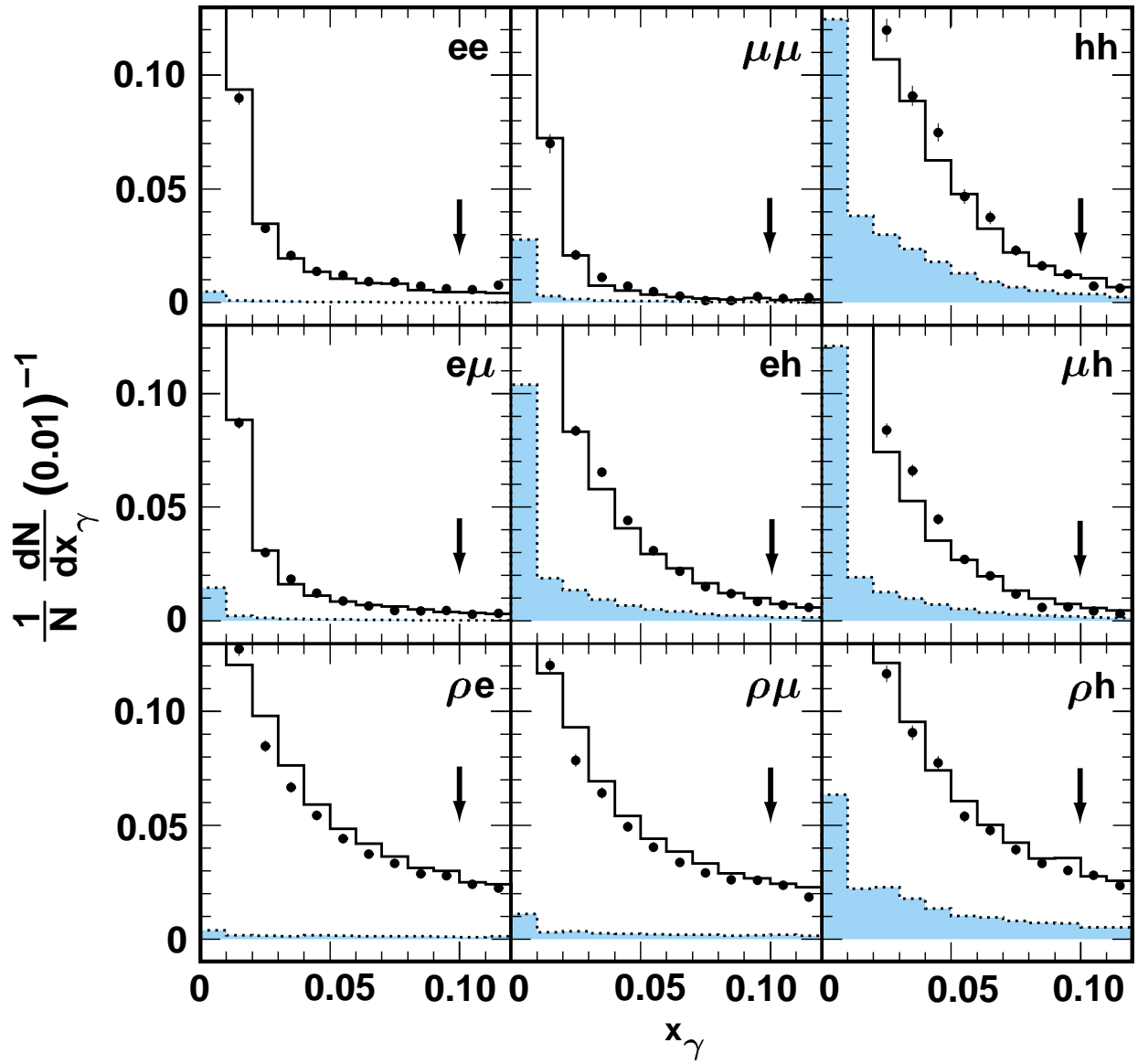
FIG. 6. Distributions in x_γ, with symbols defined as in Fig. 1.
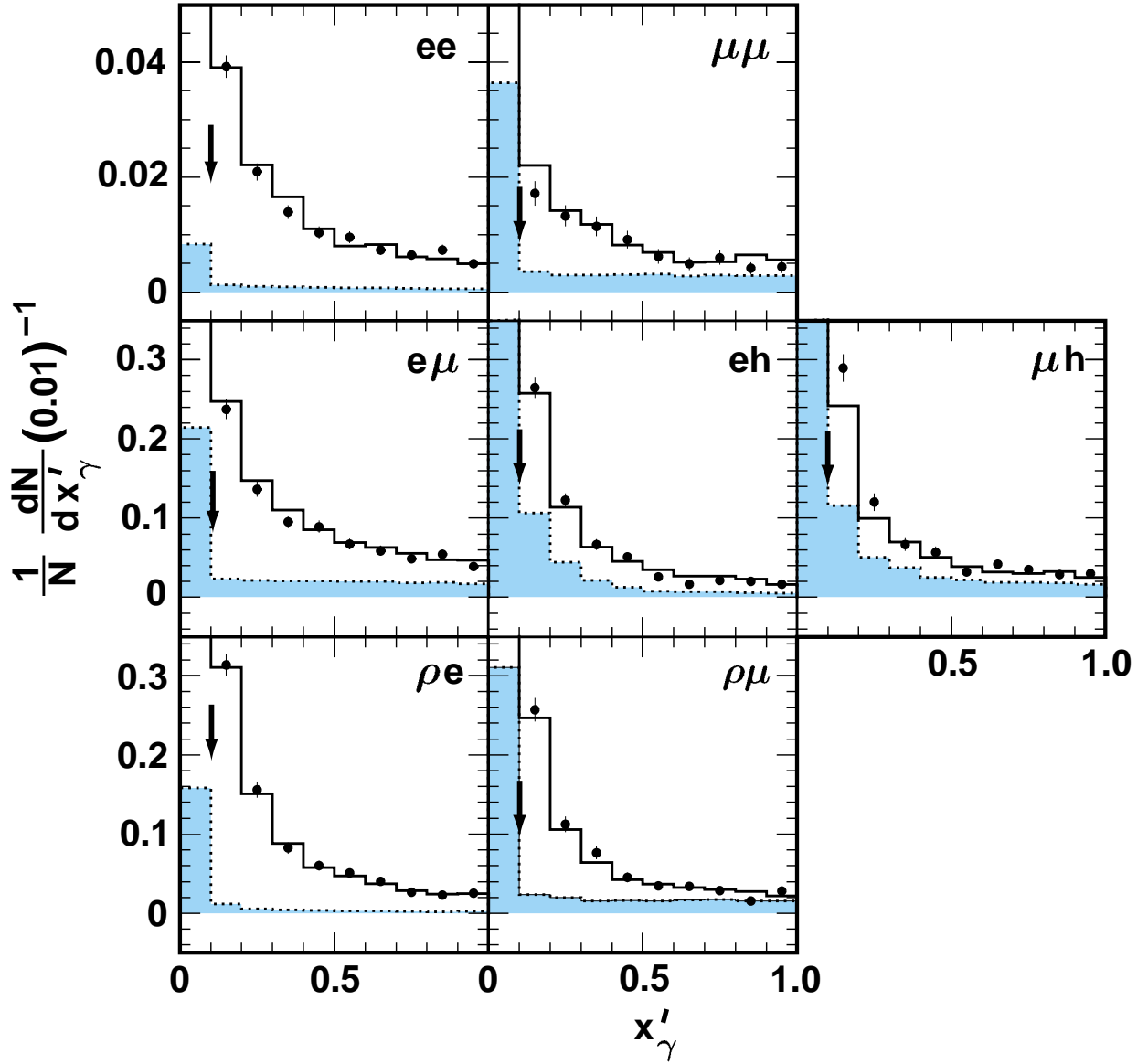
FIG. 7. Distributions in x'_γ, with symbols defined as in Fig. 1. The plot includes photons from the lepton-side(s) of the event only. This variable is undefined for hh and ρh modes.
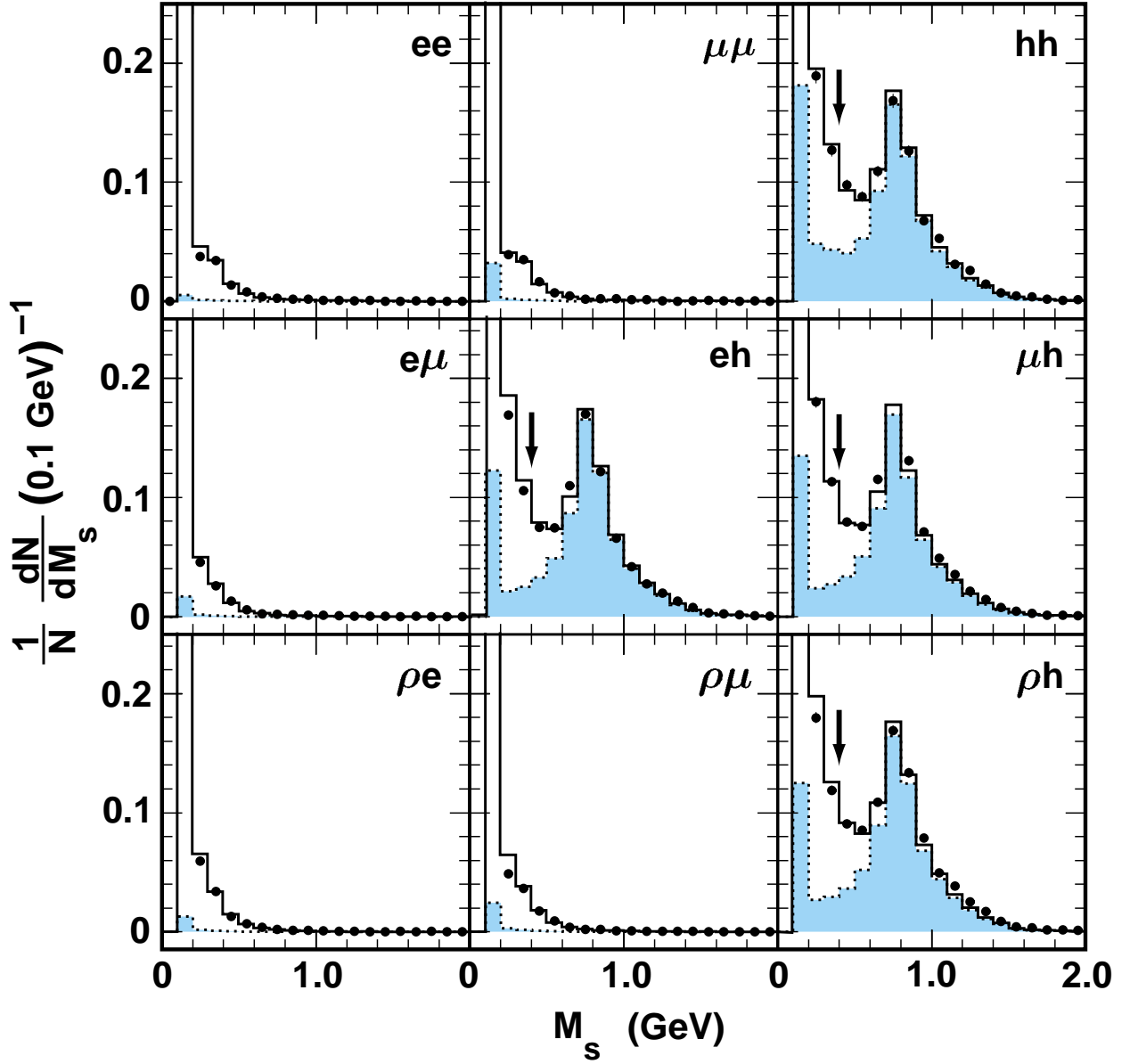
FIG. 8. Distributions in M_s for one side of the event, with symbols defined as in Fig. 1. The higher momentum track side's mass is plotted for ee, $\mu\mu$, and hh, the muon's for $e\mu$, the hadron's for eh and μh, and the track's opposite the ρ for the ρ-tag modes.
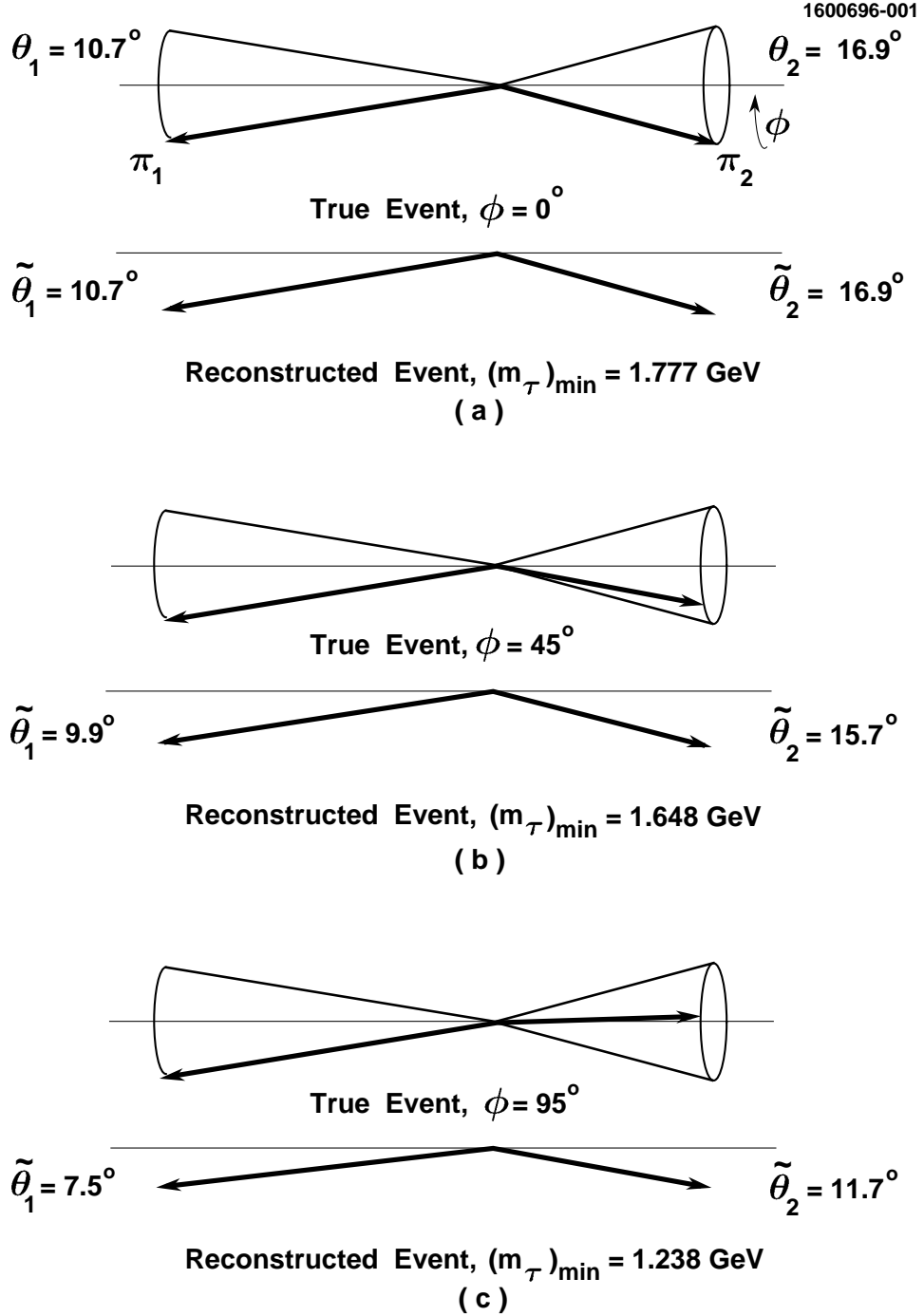
FIG. 9. A tau-pair event in which each tau decays into a charged pion (π_1 and π_2) and a neutrino (not shown). (a), (b), and (c) depict three possible directions of a 4 GeV/c π_1 and a 3 GeV/c π_2, which in all three cases have fixed polar θ_1, θ_2 with respect to the *true* tau-pair direction. The angle ϕ is here defined as angle between the π_1 and π_2 momenta when projected on a plane normal to the tau direction. For each ϕ, also shown are the corresponding values of $(m_\tau)_{min}$, as defined in the text, and $\tilde{\theta}_1$, $\tilde{\theta}_2$, angles of the pions with respect to the *reconstructed* tau-pair direction.
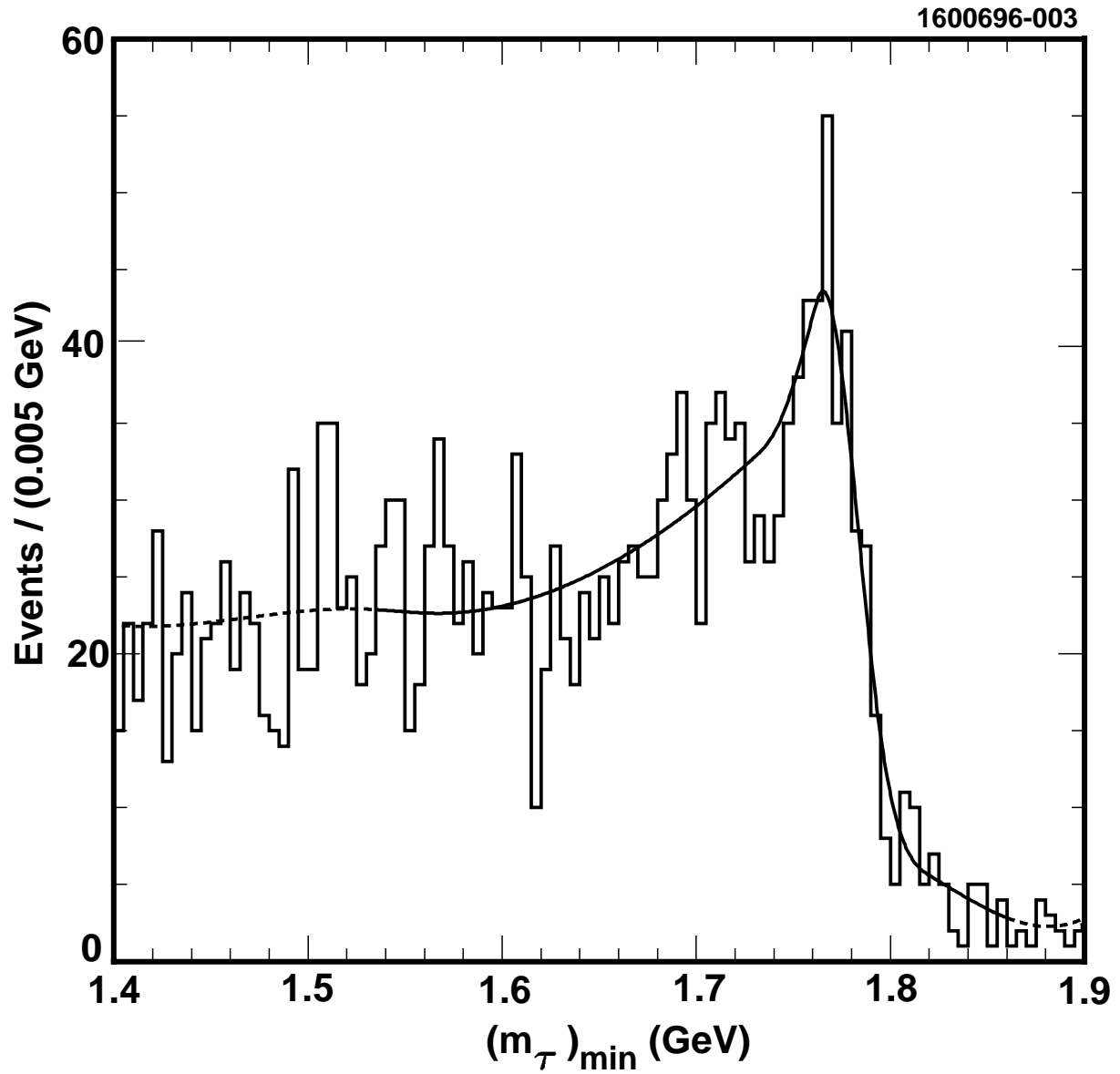
FIG. 10. Distribution of $(m_\tau)_{min}$ for the data (histogram) overlayed with the shifted and renor-malized spline curve derived from the simulation. The two fit parameters, i.e., the horizontal shift and normalization, were determined only over the solid portion of the curve (1.54-1.86 GeV).
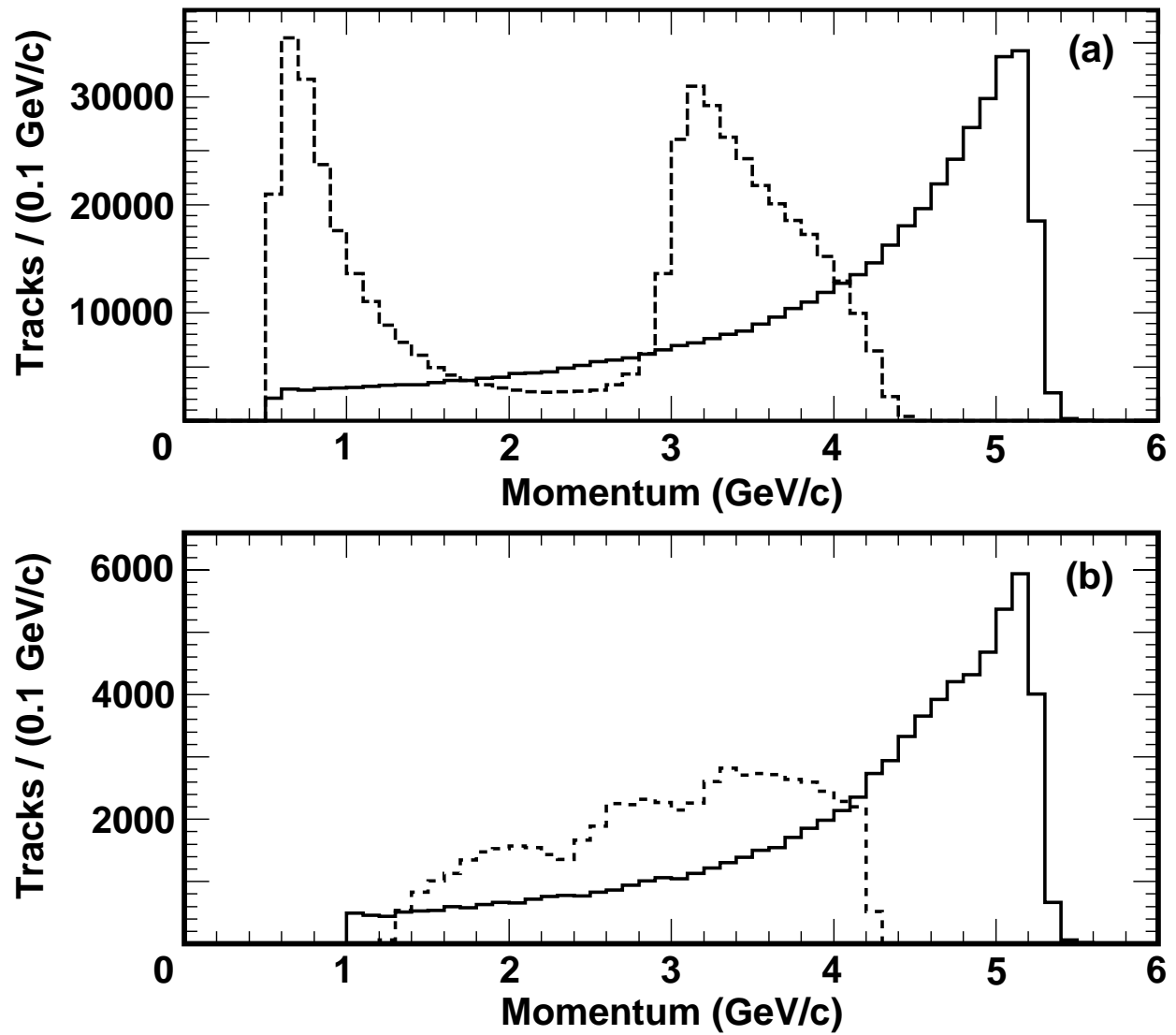
FIG. 11. Momentum spectra for tracks in candidate leptons in $\ell\ell\gamma$ (solid histograms) and $\ell\ell X$ (dashed histograms) samples, for (a) electrons, and (b) muons.
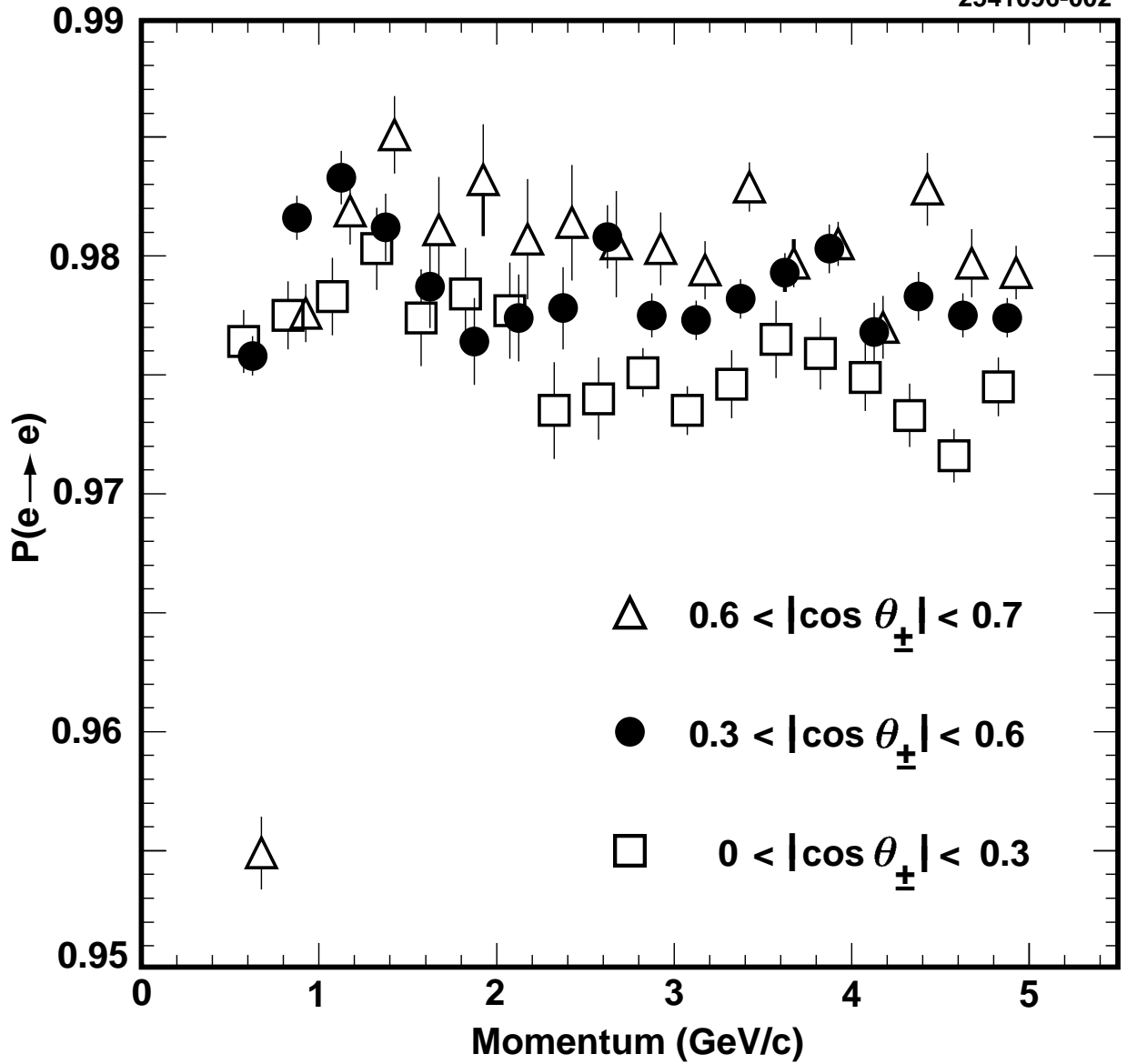
FIG. 12. Measured electron identification probability $P(e{\to}e)$ as a function of track momentum for polar angle bins $0.0{<}|\cos\theta_{\pm}|{<}0.3$ (open squares), $0.3{<}|\cos\theta_{\pm}|{<}0.6$ (solid circles), and $0.6{<}|\cos\theta_{\pm}|{<}0.7$ (open triangles). Errors bars show statistical errors only.

40
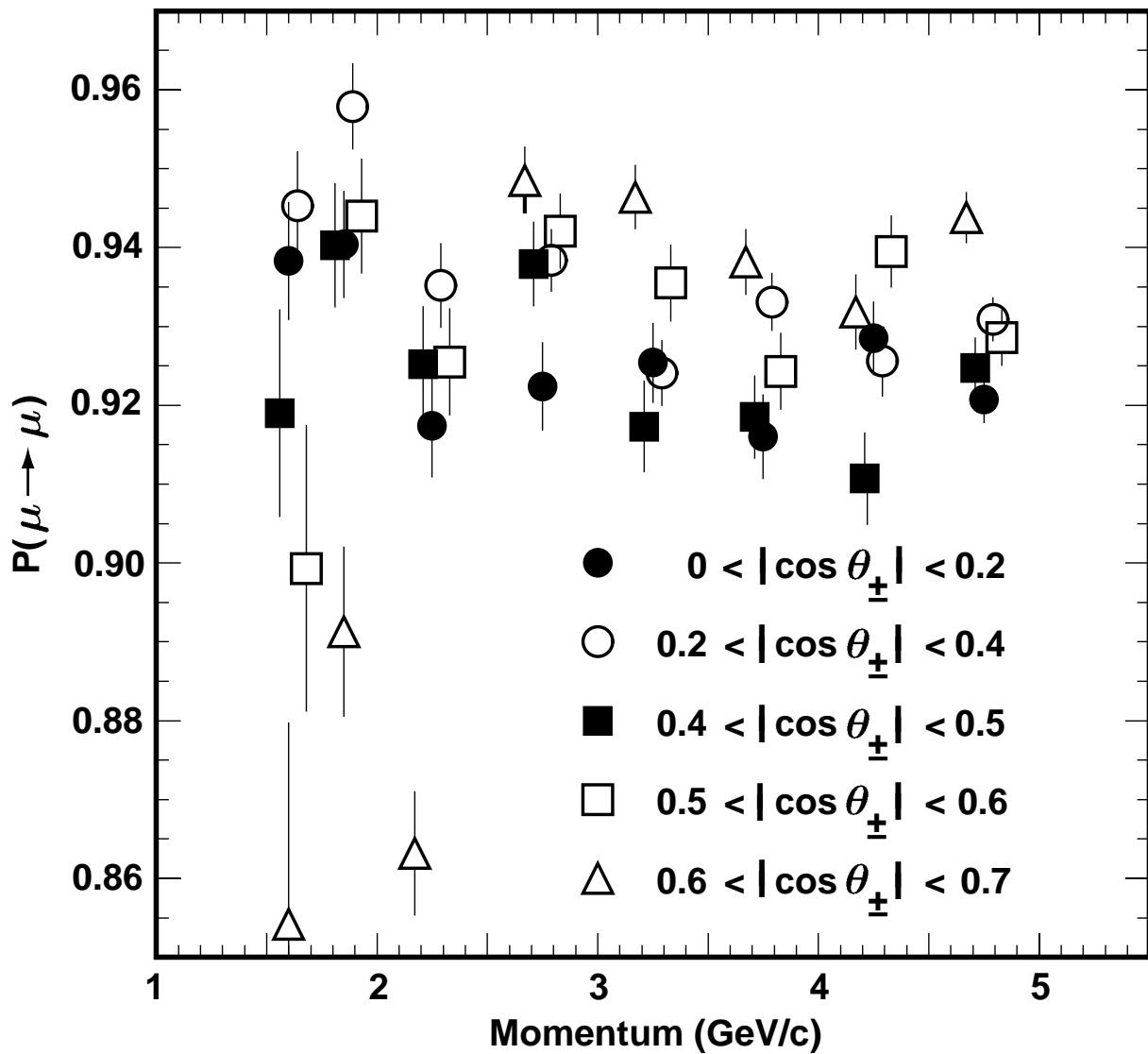
FIG. 13. Measured muon identification probability $P(\mu \rightarrow \mu)$ as a function of track momentum for polar angle bins $0.0 < |\cos\theta_\pm| < 0.2$ (solid circles), $0.2 < |\cos\theta_\pm| < 0.4$ (open circles), $0.4 < |\cos\theta_\pm| < 0.5$ (solid squares), $0.5 < |\cos\theta_\pm| < 0.6$ (open squares), and $0.6 < |\cos\theta_\pm| < 0.7$ (open triangles). Errors bars show statistical errors only.
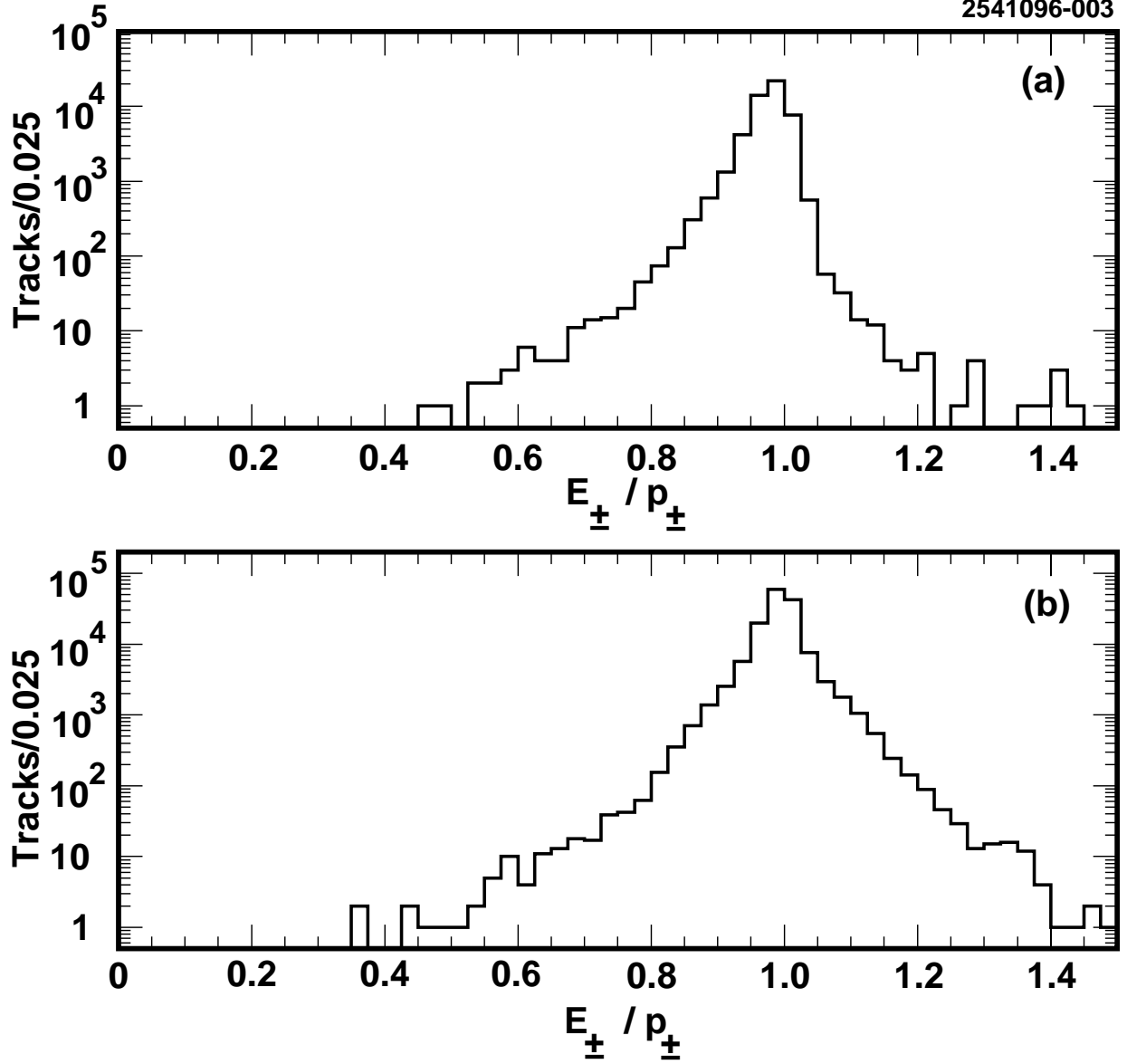
FIG. 14. Distributions in $E_\pm/p_\pm$ for tracks in $ee\gamma$ and eeX events for (a) $p_\pm$=1.0-1.5 GeV/c and (b) $p_\pm$=3.0-3.5 GeV/c .
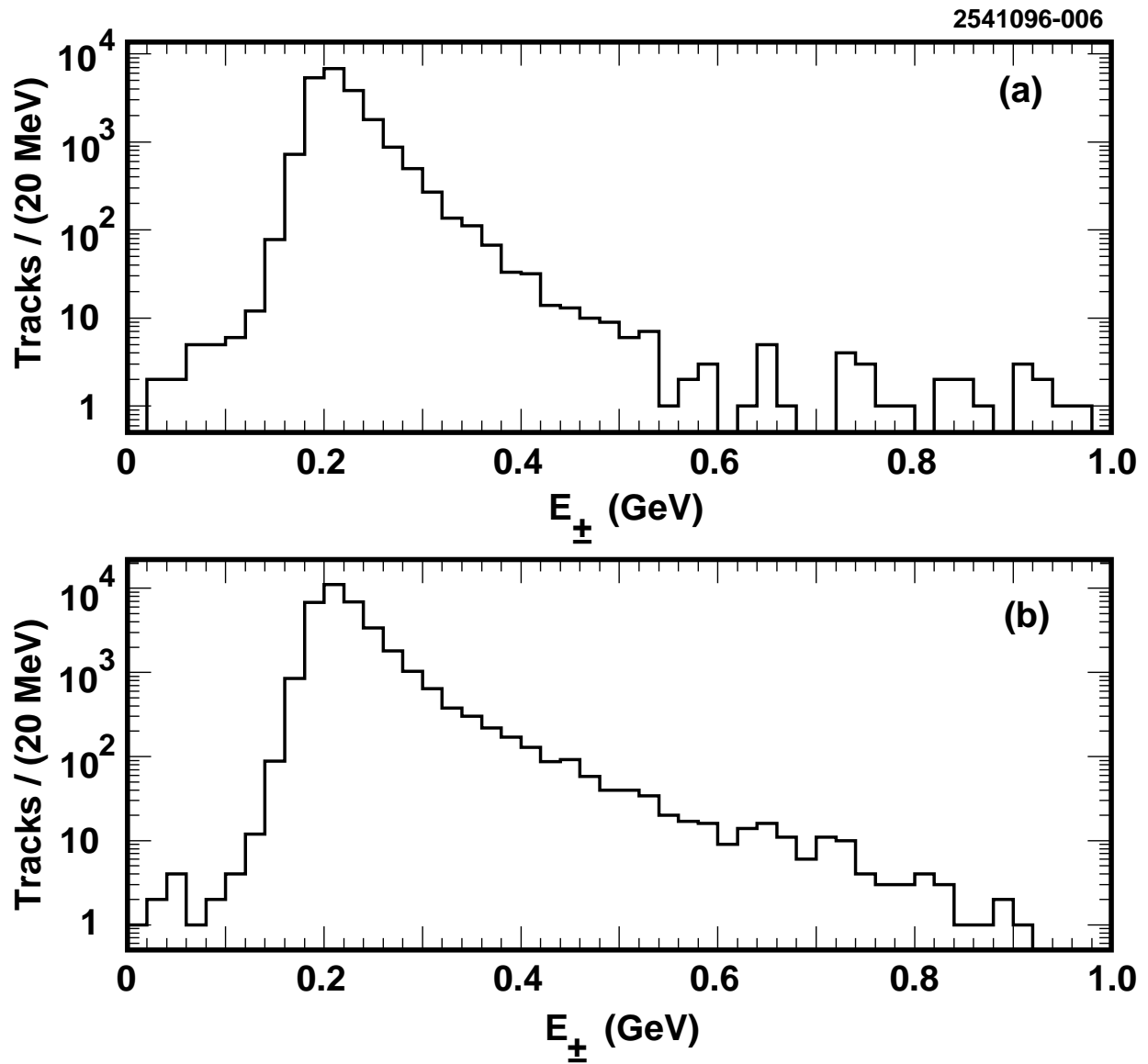
FIG. 15. Distributions in $E_\pm$ for tracks in $\mu\mu\gamma$ and $\mu\mu X$ events for (a) $p_\pm$=1.5-2.5 GeV/c and (b) $p_\pm$=2.5-3.5 GeV/c.
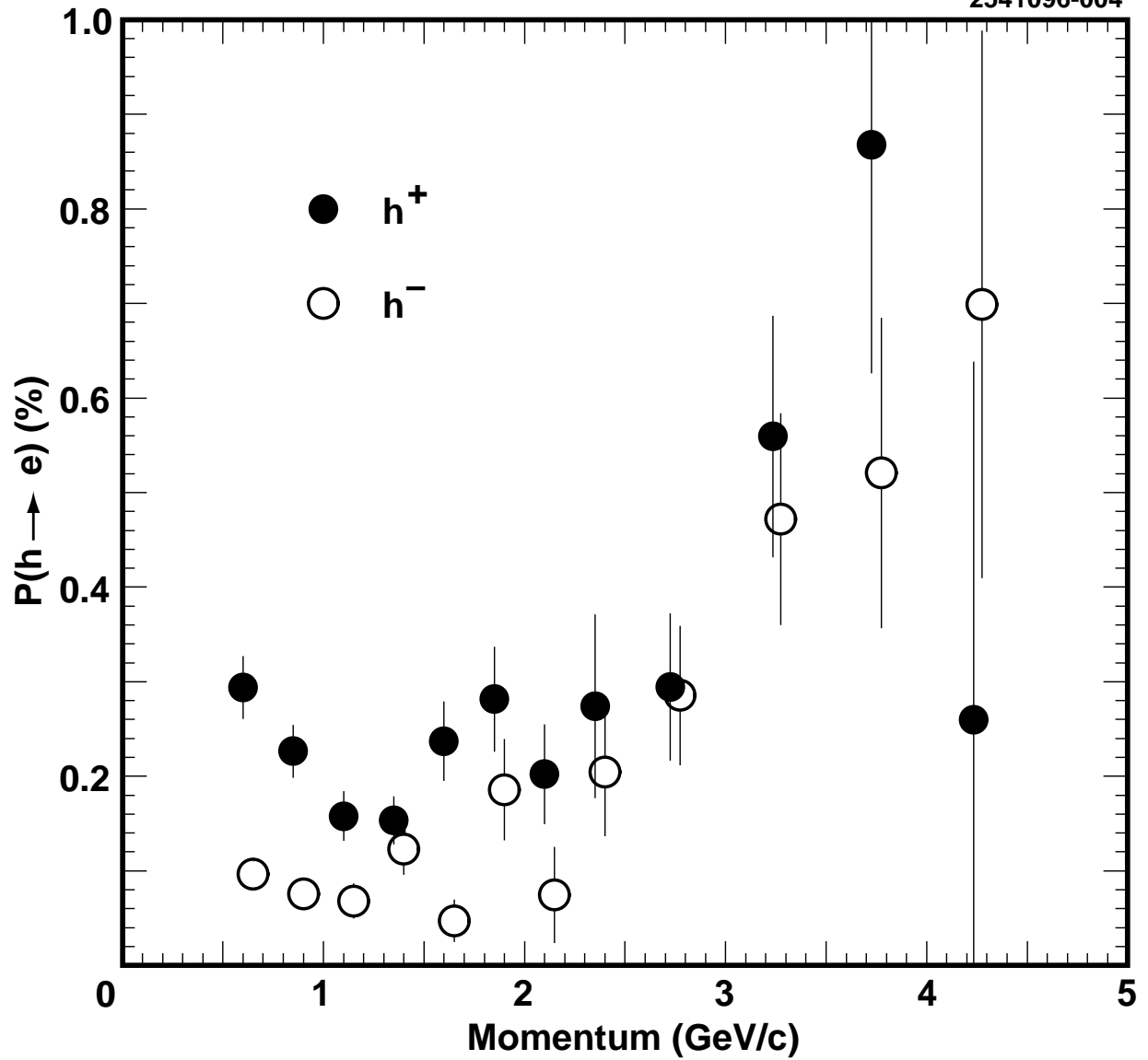
FIG. 16. Probability for a hadron to be identified as an electron as a function of momentum for positive (solid circles) or negative (open circles) charge. Errors bars show statistical errors only.
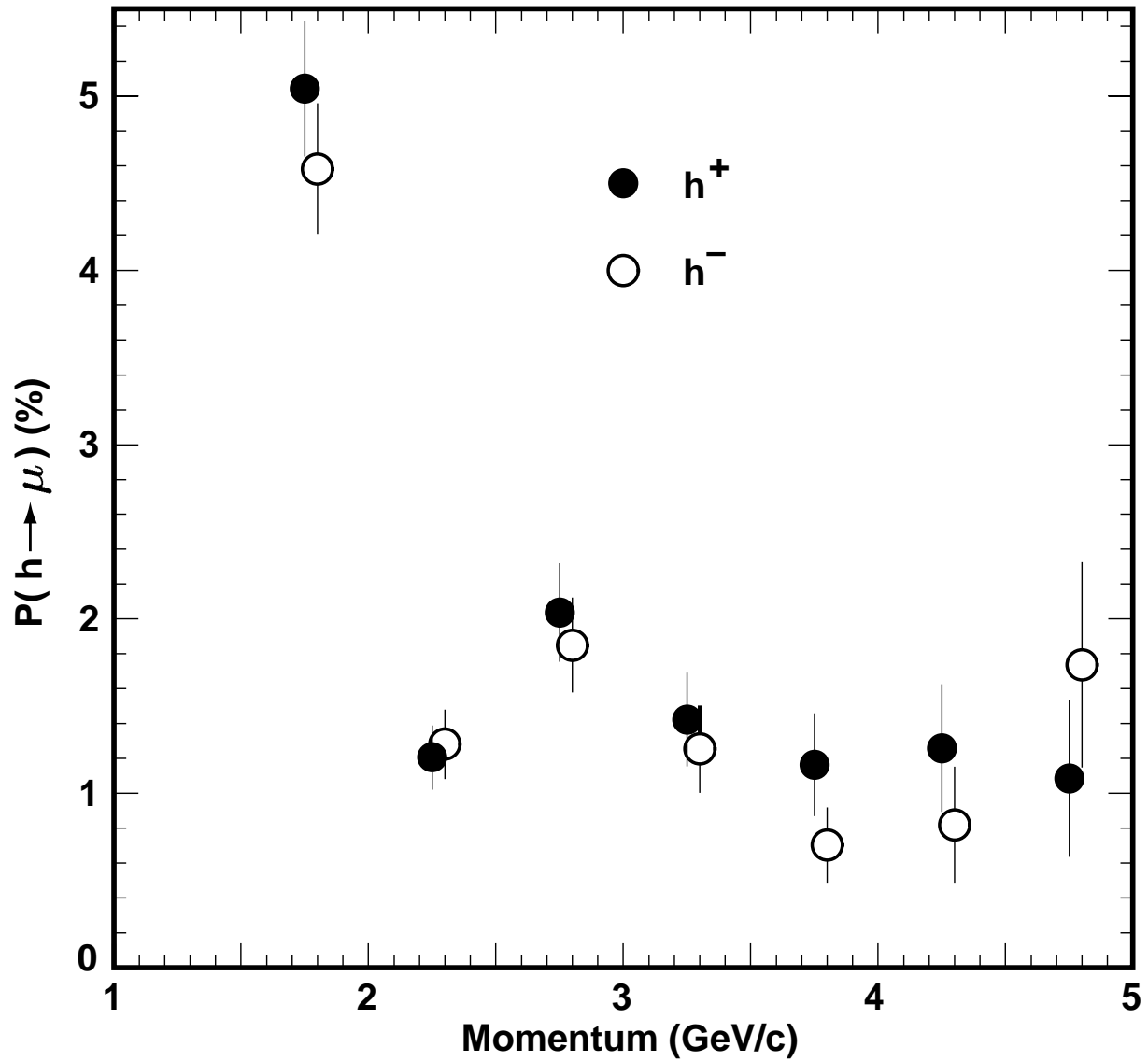
FIG. 17. Probability for a hadron to be identified as a muon as a function of momentum for positive (solid circles) or negative (open circles) charge. Errors bars show statistical errors only.